Physics – Uspekhi **62** (9) 892 – 909 (2019)

REVIEWS OF TOPICAL PROBLEMS

PACS numbers: 42.70.Df, **47.20. – k**, 47.63.Gd

Topological defects in active liquid crystals

I S Aranson

DOI: https://doi.org/10.3367/UFNe.2018.10.038433

Contents

Abstract. A wide class of nonequilibrium systems comprising interacting self-propelled agents is termed active matter. The most relevant examples include suspensions of microscopic swimming organisms (bacteria, sperm cells, or unicellular algae), synthetic catalytic nanomotors, colloidal self-propelled Janus particles, and even macroscopic bird flocks, fish schools, or human crowds. The simplest and most studied realization of active matter is a suspension of microscopic swimmers, such as motile microorganisms or self-phoretic colloids. A liquid crystal, a highly-structured anisotropic environment with local molecular ordering 'doped' by a small amount of active component represents an interesting class of nonequilibrium materials with novel optical and mechanical properties. Singularities of local molecular orientation, or topological defects, play an important role in the spatiotemporal organization of active liquid crystals. This study surveys the most recent experimental and theoretical advances in the field of active liquid crystals and highlights connections with other nonequilibrium physical and biological systems.

Keywords: microswimmers, liquid crystals, topological defects, active matter, collective motion

1. Introduction

1.1 Realizations of active matter

Active matter is a rapidly expanding field of interdisciplinary science dealing with collective and individual behavior of self-propelled agents [1–4]. These agents, both living and synthetic, may differ in nature, size, or mechanism of propulsion, and range from suspensions of micro-organisms like motile bacteria, unicellular algae, or sperm cells [5–8], cytoskeletal biological filaments and protein motors [9–11], and synthetic self-phoretic colloids [12–14] to insect swarms [15], bird flocks [16], fish schools [17], and even human crowds [18].

Among the wealth of nonequilibrium systems, active suspensions, i.e., suspensions of swimming bacteria or synthetic nanomotors, have received enormous attention. Active suspensions represent probably the simplest and most characterized realizations of active matter. Extensive experimental and theoretical studies performed by many groups all over the world have revealed the onset of collective behavior and 'bacterial turbulence' [5, 6, 19–23], a reduction in the effective viscosity [24, 25], active clustering [13], artificial rheotaxis (upstream movement) [26, 27], and many other phenomena not present in equilibrium colloidal suspensions [28]. For example, large-scale collective motion in concentrated bacterial suspensions, termed 'bacterial turbulence', is characterized by recurring intermittent vortices and jets with the spatial scale of about 50 μm. In contrast to high Reynolds number turbulence, fluid inertia in bacterial collective motion is negligible, and the corresponding Reynolds number is vanishingly small, $\mathrm{Re} \sim 10^{-3}$ [5, 6].

An accepted point of view is that the above phenomena arise due to an interplay of the following fundamental physical mechanisms: energy injection at a microscopic scale due to self-propulsion of individual agents, short-range steric collisions, and long-range hydrodynamic interactions. Another important mechanism affecting the onset of collective behavior is related to random reorientations of individual microswimmers. The origin of the noise can be related to thermal fluctuations or can be caused by intrinsic nonequilibrium mechanisms, such as the random tumbling of a bacterium [29], flipping of a synthetic gold-platinum nanorod propelled by the catalysis of hydrogen peroxide [12, 30], or random attachment kinetics of molecular motors [31].

Since the scope of active matter research became extremely broad, and the number of experimental and theoretical

I S Aranson
Departments of Biomedical Engineering, Chemistry, and Mathematics, Pennsylvania State University,
University Park, Pennsylvania 16802, USA
E-mail: isa12@psu.edu, aronson@anl.gov

Received 7 July 2018, revised 22 September 2018
Uspekhi Fizicheskikh Nauk **189** (9) 955 – 974 (2019)
DOI: https://doi.org/10.3367/UFNr.2018.10.038433
Edited by V L Derbov

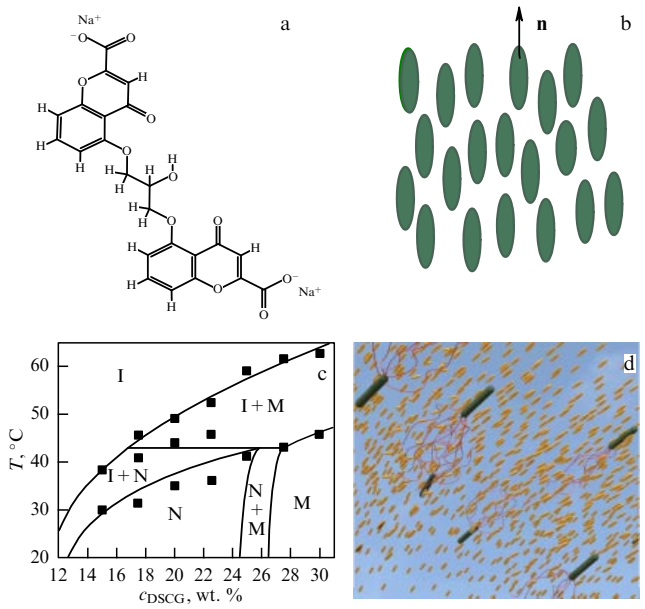

Figure 1. (a) 2D chemical structure of lyotropic liquid crystal disodium cromoglycate (DSCG). (b) In water, the disc-like DSCG molecules stack on a top of each other and self-assemble into linear rod-like aggregates. In the nematic phase, the molecules have an average orientation order characterized by the unit vector **n** (director). (c) Depending on temperature and amount of mesogenic material DSCG, the self-assembled linear aggregates form various liquid crystalline phases: nematic (N), isotropic (I), and columnar (M). (Panel c reproduced with permission from Ref. [34] © Royal Society of Chemistry 2015.) (d) Living liquid crystal is formed by a suspension of swimming flagellated bacteria in a lyotropic liquid crystal.

publications is growing exponentially, it is rather challenging to provide a comprehensive overview of the field [2, 3]. Any review paper becomes obsolete rather fast. For this reason, we mostly restrict ourselves to a rather specific but representative active matter realization, so-called active liquid crystals [32, 33]. These materials can be formed by mixing cytoskeletal filaments (microtubules) with molecular motors and crowding agents, or by combining nontoxic liquid crystal DSCG (disodium cromoglycate, $C_{23}H_{14}Na_2O_{11}$, a common anti-asthmatic drug), with motile nonvirulent flagellated bacteria *Bacillus subtilis* (see Fig. 1). The advantage of this seemingly complex system is that it is simple in preparation and experimental characterization, and amenable to a rigorous theoretical description. Namely, this system can be viewed as a composite material formed by a well-characterized equilibrium liquid crystal 'perturbed' by a small amount of an active component.

This study overviews the relevant experimental observations and various theoretical approaches to active liquid crystals and related systems.

1.2 Interactions between active particles

From the theoretical perspective, interactions between active particles can be divided into two major classes: isotropic or scalar, and anisotropic, such as polar, nematic, etc. Large-scale properties of active particles with isotropic (scalar) interactions can be effectively described by a scalar field, e.g., the particle density. The simplest realization is a self-assembly of self-propelled rigid discs or spheres, also referred to as active Brownian particles [35–37]. In such systems, the combined effect of self-propulsion and isotropic repulsion often leads to so-called motility-induced phase separation (MIPS) [38]. The simplicity of the self-propelled disc system allows mapping to an effective equilibrium theoretical system, (see, e.g., [39, 40]). The dynamics manifested by active Brownian particles are often qualitatively similar to phase-separation instability and coarsening observed in much simpler shaken granular materials, i.e., inelastically colliding macroscopic grains [41–43]. In contrast, complex shapes (rods, helices, etc.) and noncentral interactions among anisotropic particles give rise to a plethora of nontrivial dynamic collective states. Anisotropic steric, hydrodynamic, or chemical interactions among self-propelled extended objects induces nontrivial torques and forces resulting in nontrivial orientational dynamics. This behavior is illustrated by a large number of examples, such as motile bacteria in confined two-dimensional systems [6, 19, 44, 45], biopolymer motility assays [10, 11, 32], as well as shaken [46, 47] and self-propelled granular rods [48]. Furthermore, interactions among the particles can be engineered, e.g., by synthesizing patchy functionalized colloids [49, 50].

1.3 Lyotropic liquid crystals

Liquid crystals are materials exhibiting properties of solids and liquids simultaneously: they may flow like liquids but their molecules may be oriented like in crystals. As a result, liquid crystals may demonstrate both viscous and elastic response to deformations [51, 52]. A lyotropic liquid crystal is formed by dissolving an amphiphilic mesogen in a suitable solvent. Under appropriate concentration, temperature, and pressure conditions, various liquid crystalline phases are formed due to self-assembly of polar disc-like molecules of DSCG into linear nanometer-sized aggregates (so-called chromonics) [53] (Fig. 1a, b). In the simplest liquid crystalline phase, a nematic, the molecules have average orientational order characterized by the unit vector **n** (director), but no positional ordering. Since the head and tail of a molecule are indistinguishable, directions **n** and $-\mathbf{n}$ are equivalent. Nematic and isotropic phases may coexist in a certain range of temperatures and mesogen concentrations c_{DSCG} (Fig. 1c). Furthermore an increase in the concentration of the mesogenic material results in the formation of a more ordered (and often more viscous) columnar phase.

Planar and homeotropic alignment. There are various ways to align liquid crystal molecules. The alignment is called planar or homogeneous if the rod-like molecules are aligned parallel to the substrate. In contrast, if a rod-like molecule is aligned perpendicular to the substrate, the alignment is called homeotropic. There are various ways to align the molecules in DSCG, e.g., by coating the substrate with a thin film of polyamide and gently rubbing it with a velvet cloth in a certain direction [33, 54]. Homeotropic alignment is usually achieved by certain surfactants or detergents. For example, to implement a homeotropic alignment of DSCG, the glass surfaces of a liquid crystal cell are treated with a water solution containing N-dimethyl-N-octadecyl-3-aminopropyl trimethoxysilyl chloride and sulfuric acid [55, 56]. Homeotropic alignment can also be enforced by the growth of graphene monolayers on thin copper foils via chemical vapor deposition and the consequent transfer of them onto a glass substrate [57].

1.4 Topological defects

Singularities of an orientational field, or topological defects, often play a crucial role in the spatiotemporal organization of both equilibrium and active liquid crystals. In a more general context, topological defects are stable entities that form when a certain symmetry (e.g., axial) is broken at a phase transition (see review [58]).

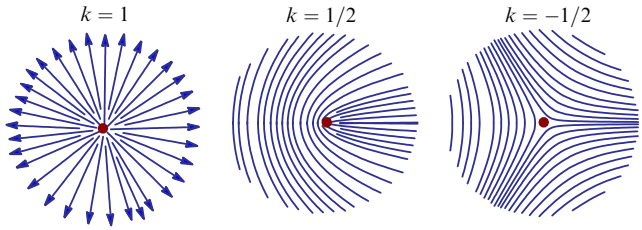

Figure 2. Topological defects for the values of topological charge $k = 1$ (a), $1/2$ (b), $-1/2$ (c); red dot depicts the singularity point.

1.4.1 Topological charge. In the context of nematic liquid crystals, topological defects are point singularities of the director field **n** [51, 52]. In two dimensions, topological defects are characterized by their topological charge k:

$$k = \frac{1}{2\pi}\oint_{\Gamma} \nabla\theta \, \mathrm{d}\mathbf{l} = \frac{1}{2\pi}\oint_{\Gamma} \mathrm{d}\theta \,, \tag{1}$$

where θ is the angle of average molecular orientation, $\mathbf{n} = (\cos\theta, \sin\theta)$, Γ is an arbitrary contour encircling the point of singularity, and **l** is the length element along the contour Γ. Topological charge measures how many multiples of 2π the director field rotates after encircling the singularity point.

The continuity condition implies that physical vector fields (e.g., magnetization or polarization) allow only integer values of the topological charge k. In nematic systems, the equivalence of $\mathbf{n} \longleftrightarrow -\mathbf{n}$ allows half-integer topological defects with $k = \pm 1/2$, or disclinations (see Fig. 2). The director reflection symmetry $\mathbf{n} \longleftrightarrow -\mathbf{n}$ makes describing a nematic rather cumbersome. In turn, topological defects in nematics are often described by the tensorial order parameter **Q** related to the director **n** via a tensorial product:

$$\mathbf{Q} = q\left(\mathbf{nn} - \frac{\mathbf{I}}{d}\right). \tag{2}$$

Here, **I** is the identity matrix, q is the scalar magnitude of the order parameter, and $d = 2, 3$ is the dimensionality of the system. Thus, **Q** is a symmetric traceless tensor. In the defect core, $q = 0$, and $q \to$ const far away from the core. The tensor **Q** is invariant with respect to reflection $\mathbf{n} \to -\mathbf{n}$. In two dimensions, the tensorial order parameter **Q** is equivalent to a complex order parameter $\psi = Q_{11} + \mathrm{i}Q_{12}$. It formally maps the 2D nematic to a class of condensed matter systems with a complex order parameter, such as type-II superconductors, superfluid helium ^{4}He, and certain pattern-forming systems [59]. Furthermore, the dynamics of half-integer defects (disclinations) become formally equivalent to the motion of Abrikosov vortices described by the Ginzburg–Landau equation [60].

1.4.2 Active defects. In equilibrium homogeneous liquid crystals, topological defects appear as a result of a phase transition. Moreover, isolated topological defects remain at rest if interaction with the boundaries is ignored. If the equilibrium is perturbed, the migration of topological defects decreases the free energy and brings the system back to equilibrium. The situation is more subtle in intrinsically nonequilibrium systems such as active liquid crystals. On the grounds of symmetry, one can argue that if the system is homogeneous, negative (i.e., triangular) defects should remain immobile due to a symmetric distribution of the active component, i.e., bacteria, microtubules, etc. In contrast, positive (or pointed) defects should move spontaneously due to nonsymmetric activity distribution [62–65] (Fig. 3).

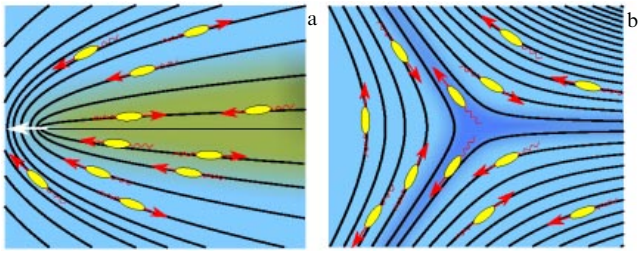

Figure 3. Half-integer topological defects in active liquid crystals. Flagellated bacteria indicate the distribution of activity, colors depict the concentration of bacteria. (a) Pointed ($k = 1/2$) defect. White arrow shows the direction of motion. (b) Triangular ($k = 1/2$) defect. (Figure is reproduced from Ref. [61] © American Physical Society (APS) 2017.)

Thus, $1/2$ defects become self-propelled entities moving typically in the direction of the pointed end (Fig. 3). Due to the interaction between the defects, negative defects may become entrained as well. However, their typical speed remains significantly lower than that of the positive ones [61].

If the activity of the system is relatively small, the dynamics of $\pm 1/2$ topological defects can be described analytically using a similarity with quantum vortices in the Ginzburg–Landau equation [59, 66]. In the presence of a weak phase (orientation) gradient $\nabla\theta_{\mathrm{ext}}$ (e.g., due to interaction with other defects or an imposed director pattern), the velocity of a defect **v** satisfies the following condition:

$$kR_{\pi/2}\mathbf{v}\left(\log\frac{v_0}{|\mathbf{v}|} + \alpha\frac{\hat{\mathbf{x}}\mathbf{v}}{|\mathbf{v}|^2}\right) = \nabla\theta_{\mathrm{ext}} \,, \tag{3}$$

where the constant $v_0 \approx 3.29$, $\hat{\mathbf{x}}$ is a unit vector in the direction of motion, the parameter α depends on the activity of the system, $k = \pm 1/2$ is the topological charge, and $R_{\pi/2}$ denotes a clockwise rotation matrix by the angle $\pi/2$ [63]. For positive defects, $\alpha \neq 0$, and for negative defects, $\alpha = 0$. Thus, for an isolated positive defect, one obtains from Eqn (3): $v\log(v_0/v) = -\alpha$, i.e., $v \neq 0$. Thus, positive defects are self-propelled (here, $v = |\mathbf{v}|$). For negative defects, Eqn (3) yields $v = 0$. In the case of several well-separated defects, the term $\nabla\theta_{\mathrm{ext}} \approx \mathbf{R}/|\mathbf{R}|^2$, where **R** is the inter-defect distance. Moreover, it is obtained that oppositely charged defects attract each other, and defects of the same sign repel each other.

Topological defects strongly influence the spatiotemporal behavior of active media. Since they cannot appear or disappear spontaneously — opposite defects are created and annihilated in pairs — the defects play the role of fundamental nonlinear excitations that orchestrate the overall dynamics of the medium.

2. Survey of experimental systems

2.1 Active nematic

An active nematic is an important and distinct class of active living material comprising nonmotile but otherwise active particles with apolar (i.e., nematic) interaction. The most successful realization of an active nematic is a mixture of kinesin molecular motors and cytoskeletal filaments —

microtubules — in the presence of biological 'fuel' (adenosine-triphosphate, ATP) and the crowding agent polyethylene glycol (PEG) [32]. The mixture is confined in a quasi-two-dimensional chamber. Individual particles (microtubules) are polar: they have distinct '+' and '−' ends. However, in the absence of active kinesin molecular motors, they remain nonmotile and only exhibit Brownian diffusion. The dynamics is drastically changed when the fuel (ATP) is introduced: hydrolysis of ATP molecules triggers conformation changes to microtubule-bound kinesin motors and directed motion of them towards the + end. Furthermore, the attachment of active kinesin clusters to a pair of microtubules of opposite polarity leads to the relative sliding and the overall displacement of the centers of mass of individual microtubules. The relative sliding induces so-called 'active stresses' on the surrounding medium and drives self-organization. The presence of PEG promotes the formation of microtubule bundles and the onset of liquid crystalline (or nematic) order [32] (see also for review Ref. [68]).

2.1.1 Long-range defect ordering. Active nematics exhibit fascinating complex spatiotemporal behavior [32], long-range ordering of topological defects [69], and nontrivial coupling between topology and activity [67]. Depending on the activity of the system (i.e., concentration of kinesin motors and amount of ATP), the system may exhibit turbulent-like states and complex streaming patterns with multiple defects (Fig. 4b). The defect dynamics is qualitatively consistent with those described by Eqn (3), at least at low activity levels.

One may expect that a turbulent-like flow in an active nematic would completely destroy all correlations among the topological defects. However, studies in Ref. [69] revealed surprising long-range orientational ordering of topological defects over centimeter-scale distances, which exceed the size of a microtubule (about 5 μm) by several orders of magnitude. By tracking thousands of defects, a long-living nonequilibrium phase characterized by a long-range orientational order of defects was observed in the experiment. Somewhat similar ordered defect textures were obtained in coarse-grained particle simulation. However, a theoretical understanding of this remarkable phenomenon is still incomplete.

2.1.2 Active nematic on curved surfaces. In addition to flat substrates, an active nematic can also be confined on curved surfaces such as spherical vesicles or tori [64, 67]. In this situation, the interplay of activity and topology leads to a number of nontrivial effects. There is a fundamental mathematical relationship between the number of topological defects and the topology of the surface. For a compact (no boundaries) surface such as a sphere or a torus, the Poincaré–Hopf theorem states that the total topological charge N is equal to surface Euler characteristic[1] χ [70, 71]. The Euler characteristic for a sphere is equal to 2, and for a torus, it equals 0. The Poincaré–Hopf theorem immediately implies that a nematic covering of a sphere will always contain at least 4 extra $+1/2$ defects, whereas the total topological charge of a torus is always zero.

[1] The Euler characteristic χ is a topological shape invariant. It is defined for the surfaces of polyhedra according to the formula $\chi = V - E + F$, where V, E, F are the numbers of vertices, edges, and faces, respectively. For any convex polyhedron, $\chi = 2$.

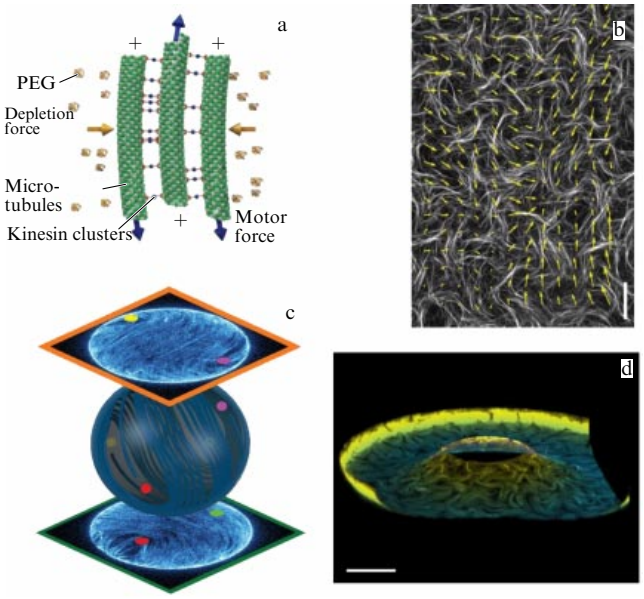

Figure 4. (Color online.) Defects in active nematics. (a) Illustration of main microscopic components of self-assembled microtubule-kinesin bundles. Kinesin clusters attach to microtubule pairs of opposite polarities and exert sliding forces. Depleting PEG polymers facilitate the formation of microtubule bundles. (b) A large-scale view of a dynamic active microtubule network. Arrows indicate the direction of the local velocity of the bundle. Scale bar 80 μm. (Panels a, b reproduced from Ref. [32] ©Nature Springer 2012). (c) Illustration of $\pm 1/2$ defect dynamics of an active nematic layer wrapped on the surface of a spherical vesicle. Image shows 3D stack of confocal slices of an active nematic vesicle. The positions of four $+1/2$ defects are shown by color dots (2 on the top plane and 2 on the bottom). (Panel c reproduced from Ref. [64] © American Association for the Advancement of Sciences 2014). (d) A confocal snapshot of an active nematic toroid. The height is shown in color code for additional clarity. Scale bar 250 μm. (Panel d reproduced from Ref. [67] © Nature Springer 2018).

Studies of an active nematic confined on the surface of a deformable spherical vesicle revealed complex spatiotemporal dynamics of half-integer topological defects (see Fig. 4c) [64]. In contrast to equilibrium systems, where defects form essentially static textures [72], here, a wealth of dynamic states was observed. For an active nematic on a torus, recent studies showed that pairs of defects unbind and segregate in the regions of opposite Gaussian curvature: positive defects are attracted to regions with positive Gaussian curvature and vice versa (Fig. 4d) [67].

2.2 Living liquid crystal

Living liquid crystal (LLC) is a composite material represented by a suspension of microswimmers like bacteria in a nontoxic lyotropic liquid crystal [33, 54, 57, 73, 74]. The material is conceived by mixing a highly-structured synthetic liquid crystal with a small amount of 'active dopant' (i.e., bacteria). An LLC exhibits unique optical and mechanical properties, such as (i) guidance of bacteria along the nematic director, (ii) visualization of nanometer-thick bacterial flagella (Fig. 5a) [33], (iii) transport of cargo along bacterial trajectories [73, 75], (iv) dynamic self-assembly of bacterial clusters [54], and (v) spinning to swimming transitions [56], etc.

A variety of fascinating collective effects is observed for higher bacterial concentrations, such as the onset of spatiotemporal director undulations, the proliferation of topological defects, and appearance of turbulent-like states [33]

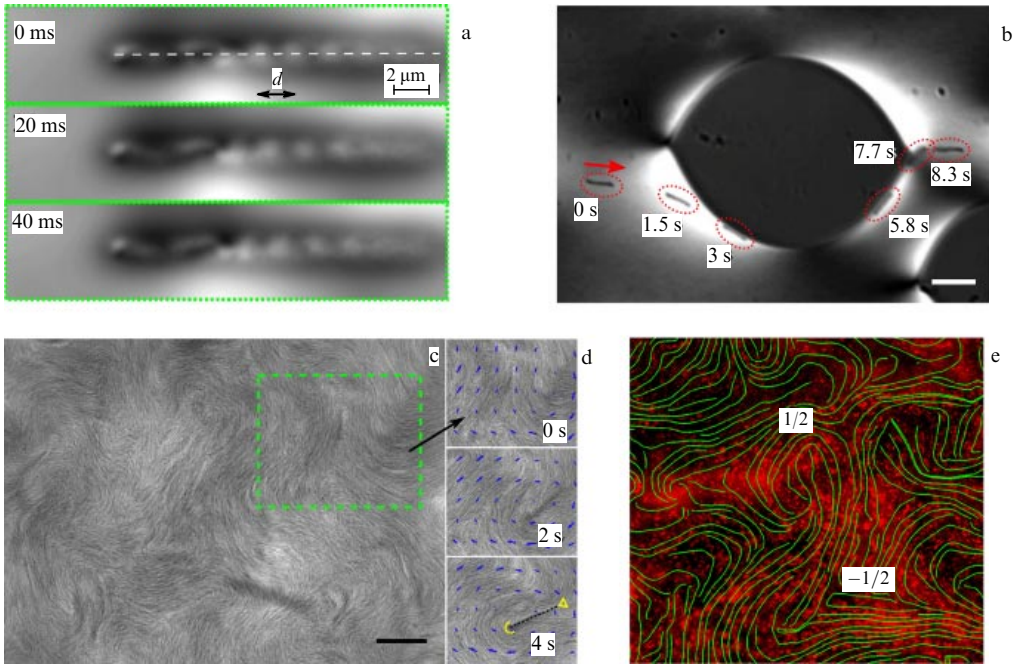

Figure 5. (Color online.) Living liquid crystal. (a) Observation of rotating bacterial flagella by polarization microscopy. Flagella thickness is about 24 nm. A sequence of snapshots illustrates rotation of bacterial flagella and counter-rotation of the bacterial body, $d \approx 2$ μm is a flagella pitch (from [33]). (See also Supplementary Movie 1 at https://ufn.ru/articles/2019/.) (b) A trajectory of a single bacterium *Bacillus subtilis* around a tactoid in an LLC. Scale bar 10 μm. (See also Supplementary Movie 2.) (c) Bright-field microscopy images illustrating the dynamic texture of topological defects formed in a free-standing LLC film [33]. Bacteria are aligned along with the local nematic director, as shown by the fine stripes. Scale bar 30 μm. (See also Supplementary Movie 3.) (d) Sequence of snapshots illustrating unbinding of a disclination pair in the domain indicated by the green box in panel (c), blue arrows show fluid velocity. (Panels a–d are reproduced from Ref. [33] © National Academy of Sciences 2014.) (e) A fluorescent image showing the distribution of bacteria and orientation of director in a free-standing film of LLC, two select defects are marked (from [61] © APS 2017).

(Fig. 5c, d). More recent studies have revealed the phenomenon of trapping and transport of bacteria in the cores of topological defects (Fig. 5a) [61] and the separation of topological defects at isotropic-nematic interfaces [76].

Active nematics (sliding microtubule systems) [32] and LLCs share many similarities in terms of the observed dynamic states and phenomena. However, the physical mechanisms governing the self-organization in these systems are very different. First, microswimmers like bacteria are self-propelled objects. As a result, the energy injection at a microscopic scale is provided by the rotation of bacterial flagella rather than the sliding of nearby microtubules. Furthermore, swimming bacteria interact with a liquid crystal by long-range hydrodynamic and elastic forces.

2.2.1 Guidance and manipulation of bacterial trajectories. Individual bacteria can be guided by a director pattern. For example, the bacteria are forced to move along isotropic-nematic interfaces [33, 54]. The isotropic and nematic phases coexist in a certain range of temperatures and mesogen concentrations (Fig. 1c). The isotropic regions appear as elongated dark droplets or 'negative tactoids' (Fig. 5b). The tactoids align along the overall nematic director [52, 53]. The tactoids distort the director and influence the trajectories of bacteria: far from the tactoid, a bacterium swims along a straight line. Near the tactoid, the bacterium deviates and follows the local distorted director. After a collision with the tactoid, the bacterium closely follows the curved isotropic-nematic interface and finally escapes at the cusp.

Spatially varying director textures can be created through surface alignment (anchoring) of the director [78, 79]. To imprint the desired director patterns, the bounding plates are pretreated to impose the desired surface alignment of the adjacent liquid crystal [78]. The procedure includes coating the plates with a layer of photosensitive molecules and consequent irradiation with a linearly polarized spatially varying light beam. The photosensitive molecules align in accordance with local polarization and force the reorientation of the director in the bulk. This imposed director pattern guides bacteria in the desired direction.

2.2.2 Active turbulence and topological defects. Spatiotemporal chaos in active systems (aka 'active turbulence') is characterized by seemingly random creation and annihilation of pairs of topological defects. Active turbulence occurs when the activity (e.g., concentration of bacteria) exceeds a certain threshold (Fig. 5c, d), [33]. In contrast to the high Reynolds number hydrodynamic turbulence characterized by an inertial range and the Kolmogorov spectrum [80], active turbulence occurs for vanishing Reynolds numbers and typically possesses a single length scale (about 50–100 μm in the case of an LLC).

A surprising phenomenon was discovered by recent experimental and theoretical studies of LLCs: $+1/2$ defects can trap bacteria in their cores, while $-1/2$ defects expel bacteria (Fig. 5a) [61]. The effect is most pronounced near the threshold of instability and the onset of active turbulence when the speed of defects is minimal. It then fades away with the increase in bacterial concentration. The phenomenon is directly related to the director distribution at the defect core. Since the bacterial trajectories that closely follow the nematic orientation converge at the core of the $+1/2$ defect, bacteria

swimming towards the defect accumulate in the core (Fig. 3a). Correspondingly, bacteria swimming in the opposite direction leave the defect. This behavior leads to an overall increase in concentration near the core. In the case of $-1/2$ defects, the nematic configuration expels the bacteria independently of their orientation (Fig. 3b): bacteria close to the defect core swim away and bacteria swimming towards the defect are deflected.

2.3 Cytoskeletal motility assays, gliding cells, and swimming bacteria

There are other systems sharing similarities with active liquid crystals and LLCs in particular. Examples include motility assays (cytoskeletal microtubules or actin filaments propelled by a carpet of molecular motors immobilized on a substrate) [10, 11, 81], living tissues of motile cells [77, 82, 83], and colonies of gliding (or creeping) bacteria such as myxobacteria [84, 85] (Fig. 6). For example, common soil rod-shaped bacteria *Myxococcus xanthus* exhibits various forms of self-organization as a response to environmental cues, e.g., starvation. Myxobacteria glide on a substrate (e.g., an agar plate) with a speed of about 2–4 μm min^{-1} and reverse their direction on average every 20 minutes.

A monolayer of close-packed gliding bacteria exhibits a liquid crystalline ordering with the dynamic textures of topological defects (Fig. 6a). Active nematic ordering is also observed in colonies of dividing bacteria confined in a monolayer [86]. In a certain limit (effective diffusion due to bacterial motility dominates fluid advection), dense suspensions of swimming bacteria can also be considered an active nematic system [101].

Another important class of systems is cultures of various motile cells, such as neuron progenitor, epithelial, stem, and cancer cells [77, 82, 83]. Depending on the cell line and experimental conditions, the cells can migrate with the speed of the order of 1 μm min^{-1}. A confluent (i.e., almost close-packed) monolayer of motile cells exhibit local nematic ordering, turbulent-like behavior, and the dynamic textures of topological defects as well (Fig. 6b).

3. Theoretical approaches

A qualitative understanding of active nematic liquid crystals can be achieved by a variety of theoretical approaches, from particle simulations to coarse-grained statistical and hydrodynamic methods. Even an incomplete list includes discrete particle models [87, 88], phenomenological models based on hydrodynamic methods [89, 90], etc. Near the onset of nematic order, an asymptotic reduction in the probabilistic Boltzmann equation for interacting particles leads to the coarse-grained Ginzburg–Landau-type model [87, 91]. Furthermore, a theoretical description based on the equilibrium model for liquid crystals [51, 52, 92] supplemented by a phenomenological 'active stress' due to mutual sliding of microtubules was introduced in Refs [62, 93–96]. These studies provided some important insights into the annihilation dynamics of defects, velocity correlations, and the onset of 'active turbulence'. However, it is not clear to what extent the 'perturbed' equilibrium model of nematic liquid crystals can be adapted for such an out-of-equilibrium system as the active nematic, how continuum models are connected to experiment [32], and how the model parameters are related to experimental conditions. In this section, we review various theoretical concepts developed in the course of understanding active nematics.

3.1 'Dry' active nematic

A certain insight into the dynamics of active liquid crystals can be obtained by studying a model system of shaken elongated granular particles, the so-called 'dry active nematic' [91]. Being much simpler than actual active liquid crystals, 'dry' active nematics exhibit nevertheless nontrivial collective behavior and the onset of large-scale spatiotemporal chaos. The chaos is manifested by the breakage and reconnection of dense, ordered, band-like structures with the local nematic order (nematic bands) [87]. Clearly, since the 'dry system' ignores long-range hydrodynamic interactions among the particles, even qualitative agreement with experiments on active liquid crystals [32, 33] is not necessarily obtained.

3.1.1 Nematic Vicsek model. The Vicsek-style model for polar self-propelled point agents [97] can be adapted to describe active nematics [98]. In this model, the point particles carry a nematic degree of freedom, align with neighbors within a certain interaction radius, and randomly change their direction under the action of an external random force. In two spatial dimensions, the algorithm is formulated in terms of positions $\mathbf{x}_j^t$ and nematic directors $\mathbf{n}_j^t \equiv \left(\cos\theta_j^t, \sin\theta_j^t\right)$ with $\theta_j^t \in [-\pi/2, \pi/2]$ of particles $j = 1, \ldots, N$. All variables are updated synchronously at discrete time steps according to the following algorithm:

$$\theta_j^{t+1} = \frac{1}{2}\arg\left[\sum_{k\in V_j}\exp\left(\mathrm{i}2\theta_k^t\right)\right] + \psi_j^t\,,$$
$$\mathbf{x}_j^{t+1} = \mathbf{x}_j^t \pm v_0\,\hat{\mathbf{n}}_j^t\,, \qquad (4)$$

where V_j is the set of neighbors of particle j within a unit distance, and v_0 is the particle speed. The function $\exp\left(\mathrm{i}2\theta_k^t\right)$

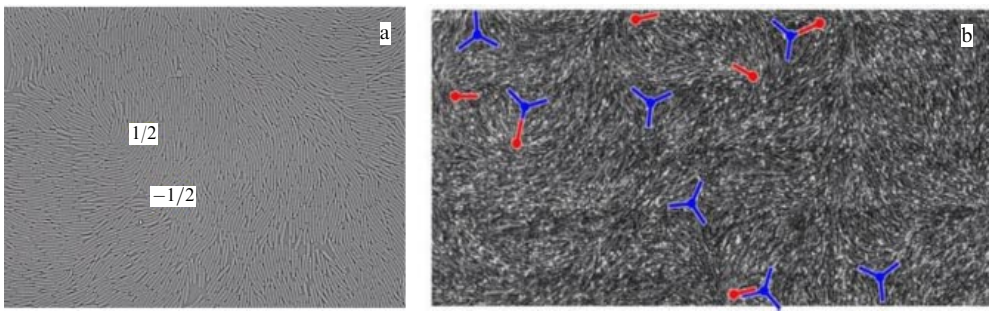

Figure 6. (Color online.) (a) Bright field microscopy snapshot of gliding bacteria *Myxococcus xanthus* with two defects indicated (from Aranson's lab). (b) Large-field image of neural progenitor cell culture. Positive $+1/2$ (red) and negative $-1/2$ (blue) defects are indicated. (From Ref. [77] © Nature Springer 2017.)

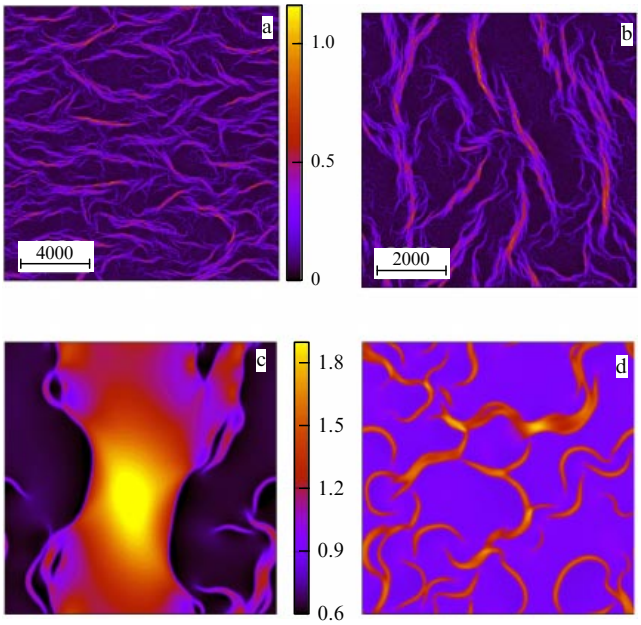

Figure 7. (Color online.) Illustration of spatiotemporal chaos in a 'dry' active nematic. (a, b) Images of coarse-grained density in the band chaos phase obtained from the nematic Vicsek model Eqns (4) for $L = 8192$ (a) and $L = 16.394$ (b) for $v_0 = 0.3, \eta = 0.038, \rho_0 = 1/8$. (c), (d) Snapshots of density field obtained from Eqns (7), (8) in a chaotic regime for $L = 1600$ and $\rho_0 = 1$: (c) localized chaos ($\sigma = 0.26$), (d) fully-developed chaos ($\sigma = 0.28$). (From Ref. [87] © APS 2014.)

in Eqn (4) implements the nematic (apolar) interaction between the agents: the outcome of interaction does not change upon direction inversion: $\theta \to \theta + \pi$. The sign in the second Eqn (4) is chosen randomly with equal probability to ensure that the particles are active but not self-propelled on a large time scale: at each time step, they can move in either direction with equal probability. Finally, independent random angles $\psi_j^t \in [-\eta\pi/2, \eta\pi/2]$ are obtained for a random variable $\eta \in [0, 1]$ picked from a uniform distribution.

In sufficiently large system with sizes $L \gg 1$ and above a certain average particle (number) density $\rho_0 = N/L^2$, Eqns (4) exhibit large-scale spatiotemporal chaos, illustrated in Fig. 7a, b. As can be seen from Fig. 7, multiple dense, curved bands of various orientations are present. The bands evolve on very long timescales: they elongate, merge, and split.

3.1.2 Continuum model of dry active nematic. Discrete Eqns (4) can be systematically reduced to a coarse-grained continuum model of an active nematic. As shown in [91], the reduced continuum equations can be derived in a simple and controlled way from Eqns (4), with all model coefficients depending explicitly on the average particle density $\rho_0 = N/L^2$ and the noise strength η. The resulting continuum model has only two independent parameters remaining after rescaling. In this approach, one assumes a dilute limit and a molecular chaos hypothesis, which allows derivation of a Boltzmann equation for the one-body distribution function $f(\mathbf{x}, \theta, t)$ [99, 100].

By expanding the distribution function f in a Fourier series of θ,

$$f(\mathbf{x}, \theta, t) = \frac{1}{\pi} \sum_{k=-\infty}^{k=\infty} \hat{f}_k(\mathbf{x}, t) \, \exp(-\mathrm{i}2k\theta) \,,$$

the kinetic approach becomes a hierarchy of coupled equations for the Fourier modes $\hat{f}_k(\mathbf{x}, t) \exp(-\mathrm{i}2k\theta)$. This hierarchy of an infinite number of equations can be truncated and closed, assuming a diffusive scaling ansatz and the proximity of the onset of nematic order. The first nontrivial order yields a nonlinear equation governing the nematic complex field $Q \equiv \hat{f}_1$, together with the continuity equation governing the density field $\rho \equiv \hat{f}_0$ [91]. Furthermore, the components of the nematic order parameter $\mathbf{Q}$ (compare to Eqn (2)) are related to the complex field Q as $Q_{xx} = \mathrm{Re}\, Q, Q_{xy} = \mathrm{Im}\, Q$. Correspondingly, $Q = Q_{xx} + \mathrm{i}Q_{xy}$. Similar equations can also be obtained in a certain limit from the kinetic theory for bacterial suspensions [101]:

$$\partial_t \rho = \frac{1}{2} \nabla^2 \rho + \frac{1}{2} \nabla\nabla : \mathbf{Q} \,, \tag{5}$$

$$\partial_t \mathbf{Q} = \mu(\rho)\, \mathbf{Q} - \frac{\xi}{2} |\mathbf{Q}|^2 \mathbf{Q} + \frac{1}{2} \nabla^2 \mathbf{Q} + \left(\nabla\nabla - \frac{\mathbf{I}}{2} \nabla^2 \right) \frac{\rho}{2} \,. \tag{6}$$

Here, $|\mathbf{Q}|^2 = \mathbf{Q} : \mathbf{Q}$, the symbol ':' denotes the inner product, $\mu(\rho) = \mu'(\rho - \rho_t)$ and the transport coefficients μ', ρ_t, and ξ are positive constants depending on the noise strength η. Here ρ_t is the threshold density ρ for the onset of nematic order. However, the tensorial notations are rather cumbersome. It is more practical to deal with Eqns (5), (6) in the form adapted for the complex nematic order parameter $Q = Q_{xx} + \mathrm{i}Q_{xy}$:

$$\partial_t \rho = \frac{1}{2} \Delta\rho + \frac{1}{2} \mathrm{Re}\, (\nabla^{*2} Q) \,, \tag{7}$$

$$\partial_t Q = \left(\mu(\rho) - \xi |Q|^2 \right) Q + \frac{1}{4} \nabla^2 \rho + \frac{1}{2} \Delta Q \,, \tag{8}$$

where the complex differential operators are $\nabla \equiv \partial_x + \mathrm{i}\partial_y$, $\nabla^* \equiv \partial_x - \mathrm{i}\partial_y$, and $\Delta \equiv \nabla\nabla^*$. This form of 'dry' active nematic equations is reminiscent of the Ginzburg–Landau equation derived in the context of superconductivity or superfluidity.

3.1.3 Nematic bands. Despite its seeming complexity, Eqns (7), (8) allow an exact inhomogeneous solution in the form of a band of nematic order with density $\rho_{\mathrm{band}} > \rho_s$ surrounded by a disordered gas with $\rho_{\mathrm{gas}} < \rho_t$. The solution can be written in simple analytical form [91, 100]. Assuming that the nematic order is along x, for this solution, one obtains $\rho = R_0(y) \equiv Q_0(y) + \rho_{\mathrm{gas}}$ and

$$Q_0(y) = \frac{3(\rho_t - \rho_{\mathrm{gas}})}{1 + a \cosh\left[\sqrt{4\mu'(\rho_t - \rho_{\mathrm{gas}})}\, y \right]} \,, \tag{9}$$

with $a = \sqrt{1 - 9\xi(\rho_t - \rho_{\mathrm{gas}})/2\mu'}$, ρ_{gas} being a constant fixed by density conservation [100]. Thanks to the simple analytical form of the band solution, its stability with respect to long-wave periodic undulations along the x direction with the wavelength k can be examined analytically. The analysis, detailed in [87], shows that the undulation growth rate λ is always positive, $\lambda \sim k^2 > 0$, implying that the band solution is always unstable. However, the instability can be suppressed in small systems.

Numerical solution of Eqns (7), (8) in a sufficiently large periodic domain demonstrated that the instability of the band is initially manifested as some periodic modulation in space

and time localized along its borders, in accordance with the linear stability analysis. It eventually leads to localized chaotic behavior (Fig. 7c). With a further increase in the system sizes and integration times, it develops into large-scale spatiotemporal chaos (Fig. 7d). The chaos is manifested by slowly elongating, merging, and breaking bands.

While there is an overall good qualitative and even semi-quantitative correspondence between discrete and continuum models of dry active nematics, agreement with experiments is somewhat limited. The 'dry' active nematic approximation captures certain aspects of dense bacterial suspensions [101], colonies of myxobacteria [84], and cytoskeletal motility assays [10, 11], but is clearly not applicable to active liquid crystal experiments [32, 33]. The main reasons are the dilute approximation (only binary collisions between the particles) and omission of long-range hydrodynamic interactions.

3.2 Liquid crystals with active stress

A phenomenological approach to active liquid crystals was developed in a series of studies [62, 65, 93–96, 102, 103]. An active nematic is described by the standard equations of liquid crystal hydrodynamics [92], written in terms of a tensorial order parameter $\mathbf{Q}$ and supplemented by an active stress term. The evolution of the order parameter $\mathbf{Q}$ and the momentum $\rho\mathbf{u}$, where $\mathbf{u}$ is the fluid velocity, is governed by the following equations:

$$(\partial_t + \mathbf{u}\nabla)\,\mathbf{Q} - \mathbf{S} = \Gamma\mathbf{H}\,, \tag{10}$$

$$\rho(\partial_t + \mathbf{u}\nabla)\,\mathbf{u} = \nabla\cdot\Pi\,. \tag{11}$$

Here, tensor $\mathbf{S}$ describes the generalized advection term, $\mathbf{H}$ is the molecular field, Π is total stress tensor, and Γ is the relaxation rate. In 2D, the molecular field $\mathbf{H} = -\delta F/\delta\mathbf{Q} + 1/2\,\mathbf{I}\,\mathrm{tr}\,(\delta F/\delta\mathbf{Q})$ is derived from the variation of the Ginzburg–Landau–de Gennes free energy, which in 2D is of the form

$$F = \frac{K}{2}(\partial_k Q_{ij})^2 + \frac{a}{2}Q_{ij}Q_{ij} + \frac{c}{4}(Q_{ij}Q_{ij})^2\,, \tag{12}$$

where K is the average elastic constant and a, c are the material parameters. Total stress Π includes elastic, viscous stresses and also active stress Π^{act} due to the activity of the system.

3.2.1 Active stress. Active stress originates from the mutual sliding of microtubules in the presence of molecular motors and ATP. In a certain approximation, using an analogy with dipolar stress in particle suspensions, active stress can be related to the order parameter $\mathbf{Q}$ [104, 105]

$$\Pi^{\mathrm{act}} = -\zeta\mathbf{Q}\,, \tag{13}$$

where ζ is the activity coefficient. The sign of ζ depends on the type of active system. For example, for bacterial systems (so-called pusher or extensile) and sliding pairs of microtubules, $\zeta < 0$. In contrast, $\zeta > 0$ for pullers like unicellular algae (contractile system) [21, 106].

3.2.2 Substrate friction. Since active liquid crystals are characterized by exceptionally small Reynolds numbers, the inertial term $\rho(\partial_t + \mathbf{u}\nabla)\,\mathbf{u}$ in Eqn (11) can be dropped. Moreover, active liquid crystals often interact with solid surfaces or confining plates, which results in substrate friction. Therefore, a proper friction term is needed in the linear momentum balance Eqn (11) [22, 94]. In the simplest form, substrate friction can be cast in the following form:

$$\nabla\cdot\Pi - \alpha\mathbf{u} = 0\,, \tag{14}$$

where constant α depends, for example, on the thickness of liquid crystalline film h, e.g., $\alpha \sim 1/h^2$.

Studies based on the above approach [62, 65, 93–96, 102, 103] provided a valuable insight into active liquid crystals, and even reproduced a qualitatively similar phenomenology (Fig. 8). For example, the numerical solution of Eqns (10), (14) reproduces spatiotemporal nematic textures with defects resembling experimental ones. Qualitatively similar dynamics of defects was observed as well: fast positive defects and slow negative ones. Moreover, an increase in the friction α resulted in the overall reduction in the characteristic scale and an increase in the number of defects, at least qualitatively consistent with the experiment in Ref. [107].

However, there are also limitations. First, it is not clear to what extent an equilibrium liquid crystal model corresponds to a far from equilibrium system of actively sliding microtubules [32]. Second, the expression for the active stress (13) is asymptotically rigorous for a dilute suspension of swimmers [108]. Yet, it is not clear how multi-particle interactions in dense suspensions of microtubules would modify the expression for the active stress.

3.2.3 Complex Swift–Hohenberg model. In addition to the theory of active nematics described by rather complicated liquid crystal Eqns (10), (11), somewhat simple phenomen-

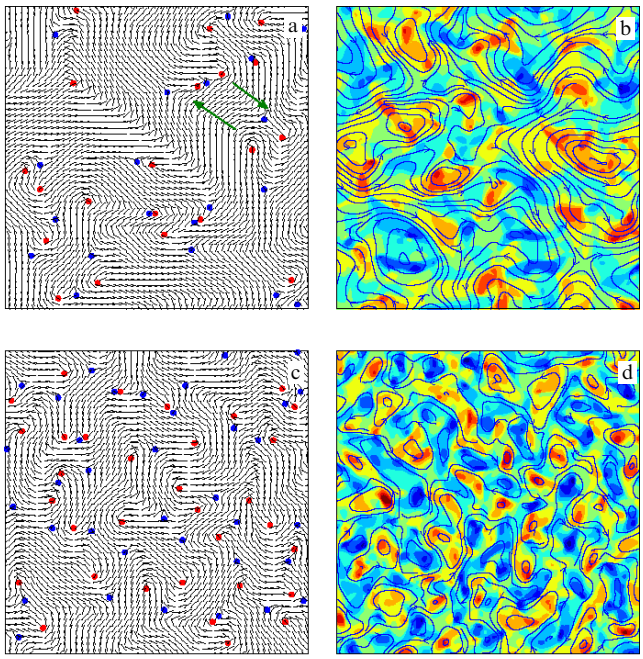

Figure 8. (Color online.) Effect of substrate friction in active liquid crystals. Panels (a, c) show director field with $\pm 1/2$ topological defects (marked by red and blue dots, respectively), and panels (b, d) show vorticity denoted by color code (from blue to red) and velocity field by arrows. Left panel: director field and topological defects (with $+1/2$ and $-1/2$ defects denoted by red and blue dots); the value of friction coefficient $\alpha = 0$ for panels (a, b) and $\alpha = 0.01$ for panels (c, d). Green arrows show the direction of motion for $+1/2$ defects. (Figure reproduced from Ref. [94] © APS 2014.)

ological models were explored as well [109, 110]. Unlike 'dry' active nematic models, they are intended to describe relatively dense phases characteristic of active liquid crystals. For example, a generalized complex Swift–Hohenberg equation was used in Ref. [110]. In the dimensionless form it is

$$\partial_t Q - D\,\mathrm{Re}\left\{(\nabla^2 Q) + \nabla Q \nabla\right\} Q = \left(\frac{1}{4} - |Q|^2\right) Q - \gamma \nabla^* \nabla Q - (\nabla^* \nabla)^2 Q\,. \tag{15}$$

Here, D, γ are the model parameters and $\nabla = \partial_x + \mathrm{i}\partial_y$. Similar equations have been used in the context of nonlinear optics, pattern formation [111], and bacterial turbulence [19]. Equation (15) exhibits a short-wave instability of the homogeneous nematic state $Q = 1/2$ and anti-polar ordering of topological defects similar to that in experiment [69]. However, derivation of this model from the discrete particle system could be challenging.

Many important aspects of active nematics can be captured by discrete particle simulations [69, 88], including active nematics on a spherical shell [112]. Discrete particle simulations are typically more time consuming than the coarse-grained continuum models and, therefore, can only describe the behavior of smaller systems.

3.3 Living liquid crystal

Since swimming bacteria are self-propelled particles, the generic phenomenological models of an active nematic [62, 93–96] are not directly applicable to LLCs. More elaborate and specialized theoretical approaches incorporating the well-established model for nematic liquid crystals [92] coupled to the concentration evolution of two populations of self-propelled particles were developed in Refs [61, 76]. Since the experiments are performed in a thin-film geometry with the scale of the emergent patterns much larger than the cell thickness h, a depth-averaged quasi-two-dimensional description is applied.

The main model assumptions are:

• *Dilute approximation*: the volume fraction of bacteria is relatively small and does not perturb the properties of the suspending liquid crystal. This assumption is justified by exceedingly small bacterial volume proportions (of the order of 0.2%) needed for the onset of instability [33]. The continuum description is valid as long as the wavelength of the emergent pattern wavelength is large compared to the inter-bacteria distance, ~ 10 μm.

• *Nematic guidance*: the suspended bacteria tend to align with the local nematic director $\mathbf{n} = (\cos\theta, \sin\theta)$, where $-\pi/2 \leqslant \theta < \pi/2$ is the nematic angle. Namely, a rod-shaped object with a planar surface anchoring, such as a bacterium, tends to align with the local director $\mathbf{n}$ [113]. The alignment of bacteria with the director happens on a time scale of a second, which is smaller than the characteristic time of the emergent collective behavior.

• *Two bacterial populations*: in a thin quasi-two-dimensional cell, bacteria traveling in opposite directions can pass without collision at slightly different heights. Thus, at each point x, y there are two concentrations of bacteria c^+ and c^-, traveling in opposite directions, $\mathbf{n}$ and $-\mathbf{n}$ (compare with [84]).

A liquid crystal is described by the standard model [92] in terms of the tensorial order parameter $\mathbf{Q}$:

$$(\partial_t + \mathbf{u}\nabla)\,\mathbf{Q} - \mathbf{S} - \Gamma \mathbf{H} + \mathbf{F}_{\mathrm{exter}} = 0\,. \tag{16}$$

Equation (16) is similar to that of active nematic Eqn (10) except for the last term, which describes the aligning effect of an external field $\mathbf{F}_{\mathrm{exter}}$. In the case of a quasi-two-dimensional thin cell, the effective force arises due to surface anchoring. Correspondingly, the equation for the linear moment balance is of the form of Eqn (14) as well. However, in contrast to the case of active nematics, all material parameters in Eqn (16) correspond to an equilibrium liquid crystal (e.g., DSCG) and are well-documented.

There is, however, a difference in the implementation of the active stress Π^{act}. A self-propelled particle, such as a motile bacterium, is a force-free object. In turns, exerting a pair of forces on the suspending fluid (force dipole or stresslet) [114]. The distribution of the force dipoles results in active stress Π^{act}, which in the dilute limit can be written as [21, 115]

$$\Pi^{\mathrm{act}} = -\Lambda c \left(\mathbf{pp} - \frac{\mathbf{I}}{2}\right), \tag{17}$$

where $\Lambda > 0$ is the force dipole magnitude imposed by the swimmer ('$-$' corresponds to pusher-type swimmers such as bacteria), and c is the concentration of bacteria. Here, $\mathbf{p} = (\cos\phi, \sin\phi)$ is the unit vector in the propulsion direction. The dynamics of bacterial orientation angle ϕ is governed by the following relaxation equation:

$$\partial_t \phi = \frac{|\mathbf{Q}|}{\tau_0} \sin(2\theta - 2\phi) + D_r \nabla^2 \phi\,. \tag{18}$$

The first term describes relaxation of the bacterial orientation angle towards the nematic angle θ with the relaxation rate $1/\tau_0$ (note nematic symmetry[2] $\theta \to \theta + \pi$). In the homogeneous nematic phase, the order parameter magnitude $|\mathbf{Q}| = \mathrm{const}$. The last term describes the diffusion of orientation with the rotational diffusion D_r. Here, it is assumed that elastic effects in a liquid crystal dominate flow alignment. This allows disregarding the advection and shear alignment terms, such as in Refs. [21]. However, this approximation breaks down in the isotropic phase, e.g., inside normal tactoids where the elastic term vanishes and $|\mathbf{Q}| = 0$ (see Section 3.4.1).

3.3.1 Angle relaxation rate. In the derivation of Eqn (18), and assuming that the angle difference is small, the relaxation towards the nematic director (due to elastic restoring torque) is taken to be proportional to the angle difference $\theta - \phi$ (see [116, 117]). This torque also has to satisfy several limiting conditions, e.g., at $\theta - \phi = \pi/2$, it has to vanish. In Eqn (18), a different form (sine of the angle difference) is used that automatically satisfies the required limiting conditions. For typical relaxation time $\tau_0 \approx 1$ s, the bacterial orientation always coincides with the director in the nematic phase, which makes the difference $\theta - \phi$ very small. Since $\sin x \approx x$ for small x, this approach is equivalent to the conventional one developed by Brochard and De Gennes [117].

The relaxation time τ_0 can be estimated from the balance of the orientation-stabilizing elastic torque and the viscous torque, $\Gamma_{\mathrm{el}} + \Gamma_{\mathrm{visc}} = 0$, by approximating a bacterium as a long rod of length l and radius r. The stabilizing elastic torque

[2] The rationale for the choice of the $\sin(2\theta - 2\phi)$ term in Eqn (18) is the following. Since $\theta - \phi$ is a periodic function, the angle relaxation has to be governed by a periodic function as well, e.g., by the sine: the leading term in the expansion of a generic periodic function.

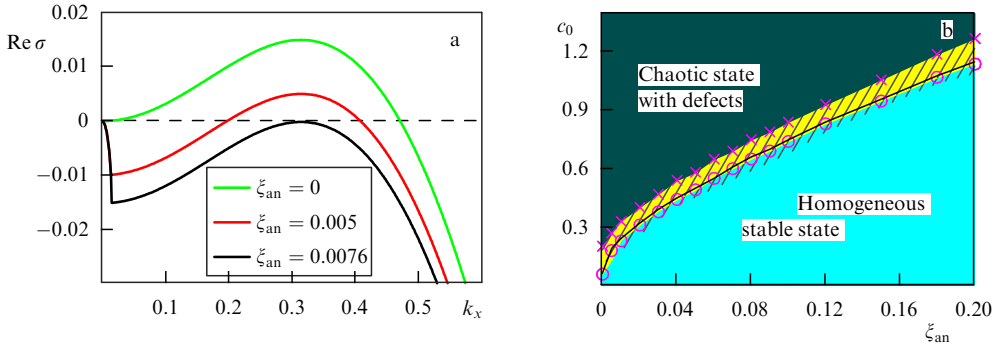

Figure 9. (Color online.) (a) Growth rate Re $(\sigma(\mathbf{k}))$ vs $k_x(k_y = 0)$ of linear periodic undulations along the nematic direction $\mathbf{n} = (1, 0)$ for different values of anchoring strength ξ_{an}, $c_0 = 0.2$. (b) Phase diagram. The black solid line indicates the linear stability limit obtained analytically. Stable director undulations exist between defect and homogeneous aligned states (bright yellow stripe). The transition boundaries are obtained by gradually increasing the average concentration c_0 from a slightly perturbed homogeneous aligned condition. Hatching shows the hysteresis domain where nonvanishing defects coexist with the periodically undulated or homogeneous aligned states. The reversal time $\tau = 66.6$ (corresponding to approximately 20–30 s for the conditions of the experiment). (Figure is reproduced from Ref. [61] © APS 2017.)

acting on a rod misaligned by an angle $\alpha = \phi - \theta$ is of the form $\Gamma_{el} = 4\pi K l\alpha/\ln(2l/r)$. Here, K is the average value of the Frank elastic constant [116]. The viscous torque is approximated as follows: $\Gamma_{visc} = \kappa\bar{\eta}\partial_t\alpha$. Here, $\bar{\eta}$ is the effective drag viscosity that depends on the director orientation and $\kappa = \pi l^3/[3(\ln(l/2r) - 1/2)]$ is the friction factor for a prolate ellipsoid [118] of an aspect ratio of approximately 7, as for a bacterium. One obtains then the relaxation time

$$\tau_0 \approx \frac{\bar{\eta} l^2}{12K} \frac{\ln(2l/r)}{\ln(l/2r) - 1/2}\,. \tag{19}$$

For typical experimental values for DSCG [119], $\bar{\eta} = 4 - 5$ kg m^{-1} s^{-1}, $K = 15$ pN, and for $l = 5$ μm, $r = 0.4$ μm, one estimates $\tau_0 \approx 1 - 1.5$ s.

Since the relaxation time τ_0 is relatively small, bacteria rapidly align with the director $\mathbf{n}$. In the following, one can assume that the vector bacterial orientation $\mathbf{p}$ is either parallel $(\phi = \theta)$ or anti-parallel $(\phi = \theta + \pi)$ to the nematic orientation $\mathbf{n}$, allowing the expression $\mathbf{pp} \to \mathbf{nn}$ to be replaced in the formulation of active stress (17).

3.3.2 Two bacterial populations. Rapid alignment of bacteria with the nematic direction allows the formulation of bacterial transport by two coupled advection-diffusion equations for the concentrations $c^{\pm}$ of bacteria swimming parallel (c^+) or anti-parallel (c^-) to the director $\mathbf{n}$:

$$\begin{aligned}
\partial_t c^+ + \nabla(V_0\mathbf{n}c^+ + \mathbf{v}c^+) &= -\frac{c^+ - c^-}{\tau} + D_c\nabla^2 c^+\,,\\
\partial_t c^- + \nabla(-V_0\mathbf{n}c^- + \mathbf{v}c^-) &= -\frac{c^- - c^+}{\tau} + D_c\nabla^2 c^-\,.
\end{aligned} \tag{20}$$

Here, V_0 is the bacterium swimming speed (about 10–15 μm s^{-1}), D_c is the diffusion coefficient, and τ is the direction reversal time. This implies that if a bacterium reverses direction, it leaves the population c^+ and joins the population c^-, or vise versa. For the most experimental conditions, the reversal time τ is typically quite large compared to the bacterial alignment time τ_0, of the order of $30 - 60$ s. The reversals are related to the run-and-tumble behavior of bacteria [29]. However, in liquid crystals, the bacteria can move only along the director because any misalignment distorts the director pattern and increases the elastic energy. Therefore, tumbling is suppressed, and only back and forth movements are permitted.

3.3.3 Phase diagram and linear stability analysis. Linear stability of the homogeneous aligned state $c^+ = c^- = c_0/2$, $\mathbf{n} = (1, 0)$ with respect to periodic undulation $\sim \exp(\sigma(\mathbf{k})t + i\mathbf{kx})$ can be investigated analytically. The growth rates $\sigma(\mathbf{k})$ vs the wavenumber $\mathbf{k}$ are shown in Fig. 9a. The instability initially occurs for perturbations with the wavevector parallel to the nematic direction, i.e., for longitudinal undulations. The most unstable wavenumber k_{cr} at the instability threshold as a function of the surface anchoring strength ξ_{an} is given by the following analytic expression:

$$k_{cr} = 2\left(\frac{3\mathrm{Er}\xi_{an}}{h^2[2\Gamma + (\xi + 1)^2]}\right)^{1/4}, \tag{21}$$

where $\mathrm{Er} = \eta V_0 l/K$ is the Ericksen number,[3] l is the bacterium length, and K is the average elastic constant. For the conditions of experiment [33], the Ericksen number is $\mathrm{Er} \approx 3.75$. $\xi \approx 1$ is the aspect ratio parameter in the Beris–Edwards theory [92]. The instability is a long-wavelength one without anchoring, i.e., it has a zero critical wavenumber at the threshold. With the increase in the concentration c, the critical wavenumber increases. However, the anchoring makes the instability a short-wavelength one with a finite critical wavenumber k_{cr} (see Fig. 9a). The critical wavenumber k_{cr} increases with the anchoring strength as $k_{cr} \sim \xi_{an}^{1/4}$ at the threshold.

Distinct dynamic regimes occurring in LLCs described by Eqns (14), (16), (20) are summarized in the phase diagram (Fig. 9b). For zero surface anchoring $(\xi_{an} = 0)$, the system remains in a stable uniform state below the critical concentration c_{cr}. An increase in the concentration c above c_{cr} results in the onset of stable periodically-undulated states, followed up by spatiotemporal chaos. As in experiment [33], the spatiotemporal chaos is characterized by chaotic-like motion, spontaneous nucleation/annihilation of topological defects, and flow generation in the liquid crystal (see Fig. 10a, d, g). This chaotic behavior is associated with a significant accumulation of bacteria in the cores of $+1/2$ defects and

[3] The Ericksen number characterizes the ratio of viscous stress to elastic stress in liquid crystals.

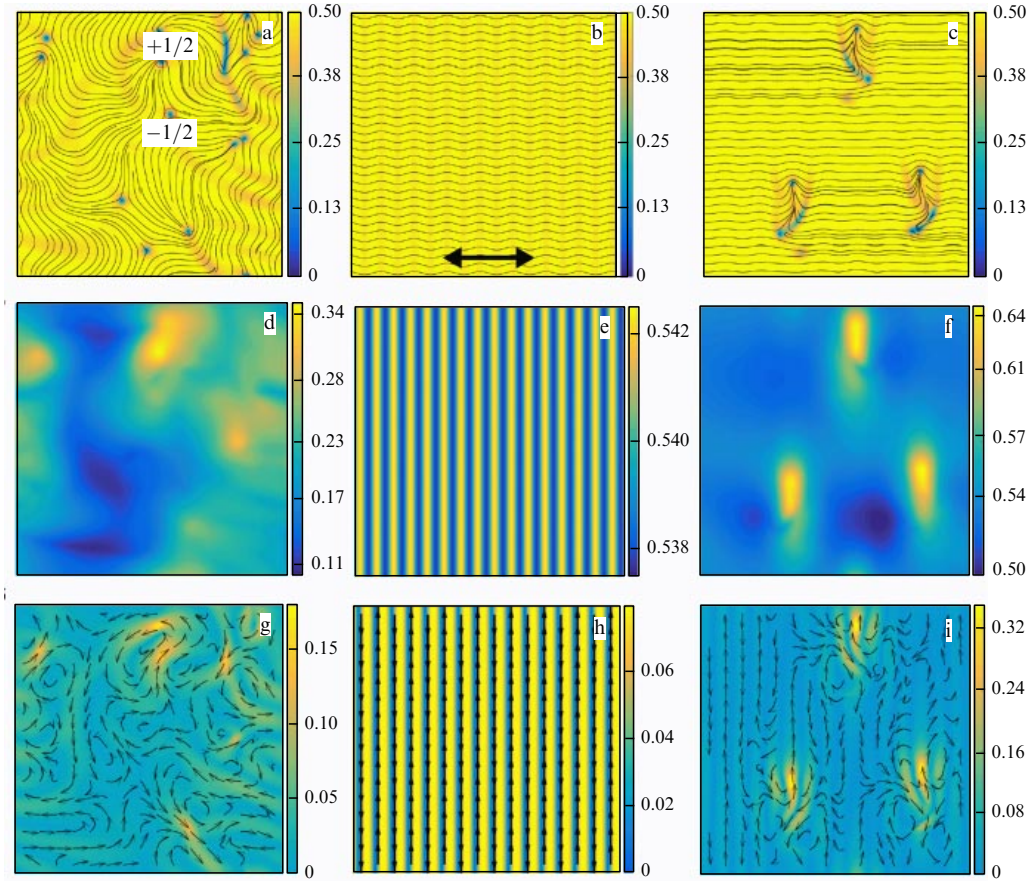

Figure 10. Nematic orientations and magnitudes of the order parameter (a–c), concentration fields (d–f), flow velocity magnitudes with streamlines (g–i). (a, d, g) Depiction of a state with defects for zero anchoring and average concentration $c_0 = 0.2$. Some $\pm 1/2$ topological defects are shown. (b, e, h) Stable periodic configuration with surface anchoring $\xi_{an} = 0.05$ and $c_0 = 0.54$, i.e., near the instability threshold. The thick black arrow indicates the prescribed director orientation set by the surface anchoring. (c, f, i) Hysteresis behavior: configuration with defects exists for the same parameter values ($\xi_{an} = 0.05, c_0 = 0.54$) as in panels (b, e, h). Other model parameters are $\tau = 66.6$, $D_c = 4$, Er $= 3.75$, $\Lambda = 1$, $\zeta = 0.2$, $\Gamma = 0.5$. See also Supplementary Videos 4–6. (Figure reproduced from Ref. [61] © APS 2017.)

the expulsion of bacteria from the cores of $-1/2$ defects (see Fig. 10d).[4]

3.3.4 Spatiotemporal chaos, hysteresis, and defect dynamics. The transition to spatiotemporal chaos is associated with a substantial hysteresis: uniformly aligned and stationary modulated states co-exist with defects for the same values of the concentration near the threshold. The main reason of the hysteresis is the accumulation of bacteria in the cores of positive defects, which, in turn, increases the local activity of the system (active stress, Eqn (17), is proportional to the concentration c). Figure 10b, e, h displays stable configurations characterized by periodic undulations of a nematic that was initially aligned along the prescribed direction. These undulations cause periodic modulation of the bacterial concentration c as well. In addition, the steady-state nematic distribution generates a sustained periodic pattern of counter-propagating flows (Fig. 10h). With a further increase in the concentration c, the periodic pattern becomes unstable and gives way to the state with moving topological defects (Fig. 10c, f, i). In contrast to the zero surface anchoring case, the defects predominantly move perpendicular to the overall nematic direction (x-axis in this case).

A characterization of defect dynamics is presented in Fig. 11. Mean defect speeds $\bar{V}$ vs the average concentration c_0 are shown in Fig. 11a. The speed of both types of defects increases almost linearly with the increase in the concentration c_0. The speed of $+1/2$ defects is higher by a factor of 5 than the speed of the negative ones. In agreement with previous studies, Refs [62, 63], an isolated $+1/2$ defect moves persistently, while the $-1/2$ one is immobile. However, due to interactions with other defects, the $-1/2$ defects become entrained by the positive ones with the speed determined by their separation distance. The speed of defects is practically independent of the anchoring strength ξ_{an} (anchoring determines only the direction of motion).

Distributions of the defect velocities $P(V)$ are shown in Fig. 11b, c. For high concentrations, the distributions $P(V)$ are well approximated by the Gaussian law $P(V) \sim \exp\left[-a_0(V - \bar{V})^2\right]$. In contrast, for lower c values, and correspondingly, for lower defect concentrations, the distributions are better approximated by a stretched exponential law,

$$P(V) \sim \exp\left[-a_1(V - \bar{V})^{\zeta}\right],$$

with the exponent $\zeta \approx 1.13$ for $-1/2$ defects and $\zeta \approx 1.4$ for $1/2$ ones. This change can be anticipated from the behavior of

[4] All parameters in the Fig. 10 caption (as well as all figure captions below) are presented in dimensionless (normalized) units, corresponding to Eqns (16)–(20). The length is scaled to the bacterium length (5 μm), the liquid velocity to the mean velocity of bacterium swimming (15 μm s^{-1}), the time to 1/3 s (the bacterium length divided by its swimming velocity). Detailed information on normalization can be found in Ref. [61].

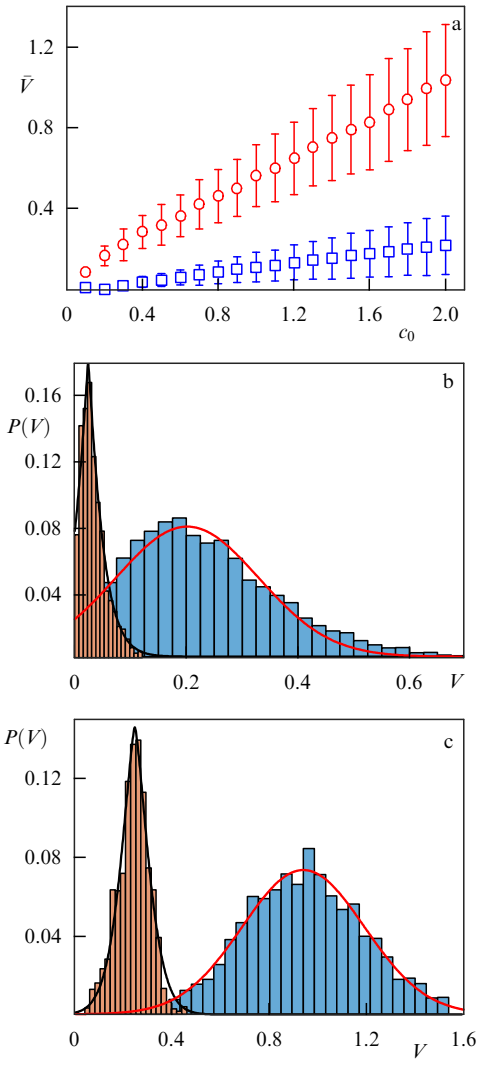

Figure 11. (Color online.) (a) Mean velocity $\bar{V}$ of $+1/2$ defects (red circles) and $-1/2$ defects (blue squares) vs c_0. Error bars are the velocity standard deviations. The velocity distributions for $-1/2$ (b) and $1/2$ defects (c) for $\xi_{an} = 0$ and for $c_0 = 1.8$ (blue) and $c_0 = 0.3$ (brown). Red solid lines are Gaussian fits, solid black lines are stretched exponential fits. (Figure is reproduced from Ref. [61] © APS 2017.)

defects at different concentrations: the defect motion is effectively randomized at high concentrations c (i.e., for high activity) leading to a Gaussian distribution. In contrast, for low concentrations, the defect dynamics is composed of long ballistic flights and rare inelastic collisions. This kind of process often exhibits non-Gaussian statistics (see, e.g., [120, 121]).

Close-up views of concentration distributions containing several moving $\pm 1/2$ defects are shown in Fig. 12. Figure 12a illustrates the accumulation of bacteria behind the core of a moving $+1/2$ defect and depletion for the $-1/2$ one.

To validate this theoretical prediction, an experiment was performed in thin films of a living liquid crystal (Fig. 12b). In this experiment, a fluorescent strain of *Bacillus subtilis* (Fig. 5e) was used to evaluate local bacterial concentrations from the fluorescence intensity. In turn, local nematic orientation was extracted from the orientation of bacteria. Overall, there is good qualitative agreement: the experiment confirmed the accumulation of bacteria in the $+1/2$ defect and depletion in the $-1/2$ defect.

The relative concentration difference $\Delta c/c_0$, $\Delta c = c_m - c_0$, where c_m is the maximum or minimal value of the concentration, decreases with an increase in average concentration c_0 or, correspondingly, activity of the system. The accumulation/depletion phenomenon vanishes in the limit of very high defect speeds [61]. In this case, the dynamics is characterized by frequent creation and annihilation of $\pm 1/2$ defect pairs. Since nearby $\pm 1/2$ defects produce the opposite trend on the concentration, the overall effect is smeared out. In addition, rapidly moving defects accumulate fewer bacteria. The accumulation/depletion also vanishes with a decrease in the bacterial reversal time τ.

3.4 Tactoids in a living nematic

In order to describe tactoids, i.e., normal inclusions, the model in Section 3.3 formulated in terms of Eqns (14), (16), (20) needs to be generalized [76]. The major difference with the above model is that the bacteria swimming direction **p** does not necessarily coincide with the nematic director **n**, because the director itself is not defined in the isotropic phase.

3.4.1 Dual nematic model. In a nematic domain, the bacterial orientation angle ϕ obeys Eqn (18). However, in a normal

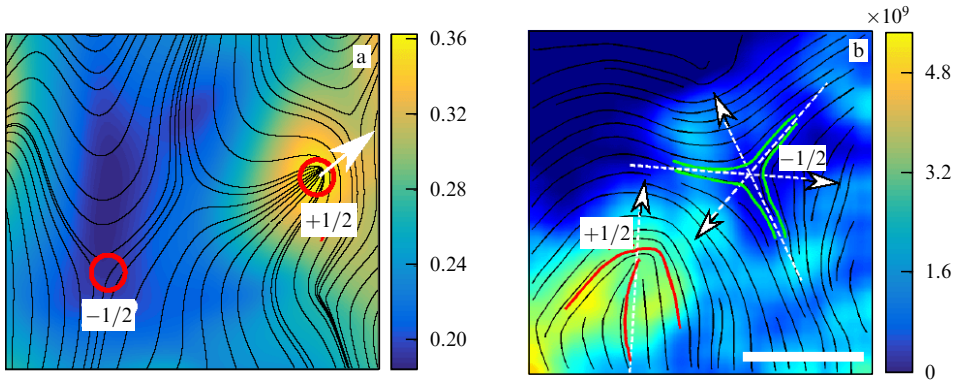

Figure 12. (Color online.) (a) Computational model: close-up view of the concentration field. Some defects are shown in red circles, white arrow indicates the direction of motion. (b) Experiment: bacterial concentration distribution in the area containing two defects. Colors represent the concentration of bacteria extracted from the averaged fluorescence intensity. Two topological defects ($1/2$ and $-1/2$) are highlighted. White lines show defect orientations. Scale bar is 50 μm. (Figure is reproduced from Ref. [61] © APS 2017.)

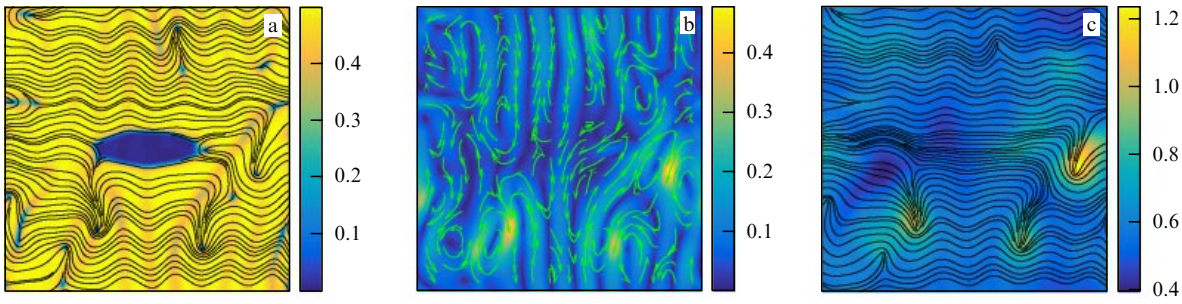

Figure 13. Isotropic tactoids in a nematic liquid. (a) Nematic contour lines and the magnitude of the order parameter, (b) fluid velocity magnitude with streamlines, (c) concentration field with bacterial orientation contour lines for wall anchoring strength $\xi_{\text{exter}} = 0.02$; planar IN anchoring strength is $\xi_{\text{anch}} = 30$, concentration $c_0 = 0.6$ (see also Supplementary Video 7). (Figure reproduced from Ref. [76] © Institute of Physics 2018.)

domain (e.g., inside an isotropic tactoid), where $|\mathbf{Q}| = 0$, the alignment term $|\mathbf{Q}| \sin(2\theta - 2\phi)$ vanishes and bacterial orientation is governed mostly by the diffusion. Since the elastic effects in liquid crystals usually dominate over the flow alignment, one can disregard the advection and shear alignment terms governing the dynamics of bacteria in a Newtonian liquid [21]. Due to angle discontinuity, Eqn (18) is difficult to solve numerically. To circumvent this problem, by analogy with the nematic tensor $\mathbf{Q}$, one can introduce an evolution equation for the traceless symmetric nematic-like tensor $\mathbf{P} = q_p(\mathbf{pp} - \mathbf{I}/2)$ constructed from the unit vector of bacterial orientation $\mathbf{p}$:

$$\partial_t \mathbf{P} = a_p \mathbf{P} - 4c_p |\mathbf{P}|^2 \mathbf{P} - \frac{\mathbf{F}_{\mathbf{Q}}}{\tau_0} + D_t \nabla^2 \mathbf{P}\,. \tag{22}$$

Here, a_p and c_p are constants controlling the amplitude $q_p = |\mathbf{P}|$. They are chosen in such way that $q_p = 1$ in the homogeneously aligned steady state.[5] The term $\mathbf{F}_{\mathbf{Q}}$ aligns tensor $\mathbf{P}$ with the nematic orientation set by tensor $\mathbf{Q}$. Here, $\tau_0 \approx 1$ s is the alignment time, which is much smaller than the bacteria reversal time $\tau \approx 60$ s [61]. The alignment term $\mathbf{F}_{\mathbf{Q}} \sim \mathbf{Q}$ is chosen in such a way that it does not change the amplitude of the tensor $\mathbf{P}$. In the limit $|\mathbf{P}| = \text{const}$, one recovers Eqn (18). Inside the tactoid, $\mathbf{F}_{\mathbf{Q}}$ vanishes, and bacterial orientation becomes independent of $\mathbf{Q}$.

In turn, the nematic tensor $\mathbf{Q}$ couples to the tensor $\mathbf{P}$ via the expression (17) for active stress. By solving Eqn (22), one determines bacterial orientation[6] $\mathbf{P}$. Correspondingly, in Eqns (20) for bacterial transport, the nematic director $\mathbf{n}$ has to be replaced by a unit vector of bacterial orientation $\mathbf{p}$.

In the isotropic-nematic (IN) coexistence domain in the phase diagram in Fig. 1c, the tactoids can be introduced in the Landau–de Gennes free energy Eqn (12) via additional term $\sim |\mathbf{Q}|^6$, in the spirit of the mean-field theory of first-order phase transitions [122]. This higher order nonlinear term makes both isotropic and nematic states locally stable. The description can be further simplified for fixed isotropic domains produced, for example, by local heating. Then, the coefficient a in front of the quadratic term in the Landau–de Gennes free energy (12) can be made spatially-dependent. It forces the equilibrium order parameter amplitude q to be a positive constant in the nematic and zero in the isotropic phase.

[5] Unlike similar terms a and c in the equation for the free energy $\mathbf{Q}$ in Eqn (12), the constants a_p and c_p are used to control the amplitude q_p of the tensor $\mathbf{P}$ only and do not bear any physical meaning.

[6] Like the nematic director, $\mathbf{p}$ and $-\mathbf{p}$ are equivalent since they are extracted from the symmetric traceless tensor $\mathbf{P}$.

To introduce an isotropic tactoid of a desired shape given by the condition $f(x, y) = 0$, one sets the coefficient a in Eqn (12) to a negative value inside the tactoid, e.g., $a = -a_2$, and to a positive value outside of the tactoid, $a = a_1$, with a rapid but continuous transition on the isotropic-nematic boundary:

$$a(x, y) = -\frac{a_1 + a_2}{2}\left[\tanh\left(-\frac{f(x, y)}{\delta}\right) + 1\right] + a_1\,. \tag{23}$$

Here, δ is the width of the isotropic-nematic interface. In order to create a nematic tactoid surrounded by an isotropic phase, the sign of the coefficient a is changed to the opposite one in the entire computational domain. In this simplified approach, the tactoid shape is predefined by the function $f(x, y)$. However, some local shape adjustments may take place near the surface defects, or boojums (see Fig. 13a). A more complicated model [95] of the biphasic system with the possibility of shape evolution can be considered as well.

The anchoring of director $\mathbf{n}$ on the isotropic-nematic interface can be implemented via an additional surface term $\mathbf{F}_{\text{anch}}$ with the corresponding anchoring strength ξ_{anch}. The form of this term is similar to that of $\mathbf{F}_{\text{exter}}$ in Eqn (16) [76]. A vector $\mathbf{f}$ of the 'easy direction' along the isotropic-nematic interface [53] is obtained from the gradient of the order parameter magnitude $\mathbf{f} \sim \nabla|\mathbf{Q}|$ (since this vector is perpendicular to the isotropic-nematic interface). This allows implementing both planar and homeotropic alignments at the isotropic-normal interface [76].

3.4.2 Charging of tactoids. A snapshot of an isotropic tactoid in the nematic phase with planar anchoring is shown in Fig. 13. At sufficiently low bacterial concentrations and high wall anchoring (wall anchoring prescribes the overall nematic orientation), an aligned regime with the nematic orientation parallel to the anchoring direction was observed. However, planar isotropic-nematic anchoring on the tactoid surface forces the nematic orientation to deviate from the horizontal one. For bacteria concentrations that are not too high, the configuration is characterized by periodic nematic undulations due to the onset of short-wave instability characterized by Eqn (21) (see Fig. 10b). The interplay of wall anchoring at the isotropic-nematic interface and the bulk nematic orientation results in a nonsymmetric flow structure around a tactoid [76]. For even higher bacteria concentrations, a chaotic regime with multiple topological defects was observed (Fig. 13). The defects enter and leave the tactoid in a random fashion and temporarily distort the planar anchoring at the isotropic-nematic interface.

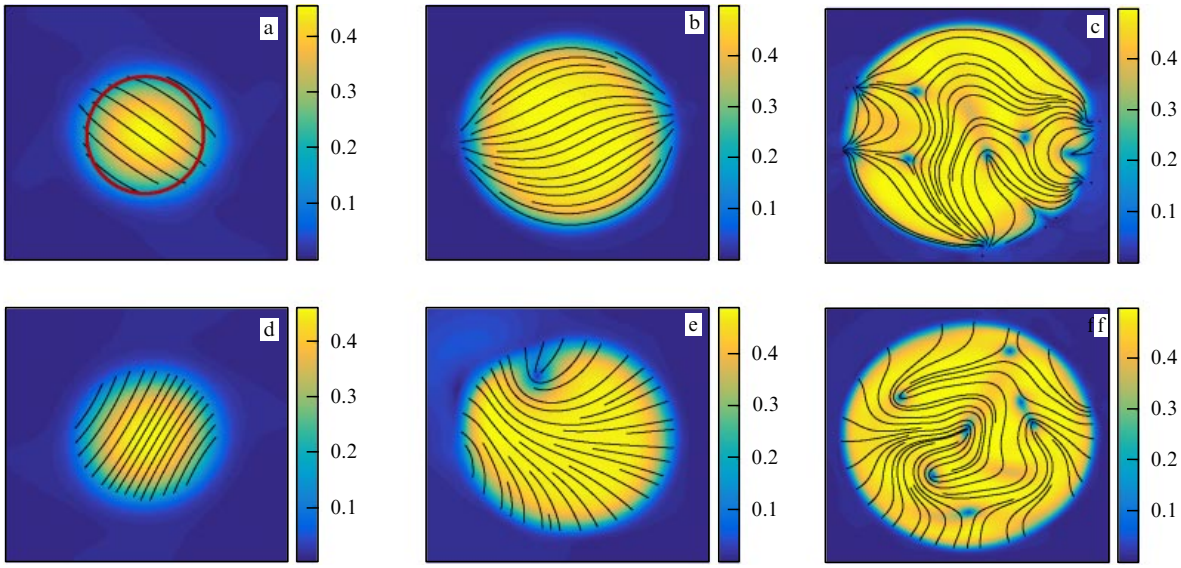

Figure 14. Nematic field configurations for fixed $c_0 = 0.6$ and different nematic tactoid sizes: planar (a) and homeotropic (d) IN anchoring for $R = 30$, planar (b) and homeotropic (e) IN anchoring for $R = 90$, planar (c) and homeotropic (f) IN anchoring for $R = 240$. No wall anchoring $\xi_{\text{exter}} = 0$ was imposed, whereas planar IN anchoring had strength $\xi_{\text{anch}} = 30$. (Figure reproduced from Ref. [76] © Institute of Physics 2018.)

Nematic tactoids in the isotropic phase are introduced by changing the sign of the Landau–de Gennes coefficient a in the entire computational domain [see Eqn (23)]. Various nematic configurations for bacteria concentrations and tactoid sizes, for both planar and homeotropic anchoring, are shown in Fig. 14. The obtained configurations are in good qualitative agreement with experiment [53]: for small tactoid sizes, the elastic forces dominate over surface anchoring, which corresponds to an almost aligned (undisturbed) nematic configuration (Fig. 14a, d). For larger sizes, there are a few singularities on the tactoid surface (Fig. 14b, e). A spindle-like configuration (so-called '2c') is observed for a larger tactoid with planar wall anchoring (Fig. 14b). These '2c' configurations with 2 positive boojums (topological defects at the nematic-isotropic interface) frequently arise in experiments [53, 123]. While the overall tactoid shape was predefined (disk), local shape adjustments near the boojums were observed. For even larger tactoid sizes, configurations with many defects are observed, both inside the tactoid and on its surface (Fig. 14c, f).

Topological defects entering/leaving a tactoid change its total topological charge and local concentration of bacteria. The charge can be extracted from the phase winding in the counterclockwise direction over a region enclosing the tactoid. The time-averaged total topological charge of the tactoid s_t and averaged relative bacteria concentration inside the tactoid c_t are calculated over the entire span of the numerical experiment. The dependences of topological charge s_t on wall anchoring and bacteria concentration c are shown in Fig. 15a, b (planar anchoring). For small bacteria concentrations and strong wall anchoring, there are no topological defects, and the tactoid's topological charge is zero. For higher concentrations, in the regime with defects, the average topological charge of the tactoid is always negative. The charge magnitude first increases with the increase in bacterial concentration but then saturates and falls. The magnitude of the tactoid's charge increases with the wall anchoring. There is also a minor suppression of relative bacterial concentration inside the tactoid. The magnitude of s_t grows almost linearly with the tactoid size. Thus, the charge density, i.e., the total charge normalized by the tactoid length, remains practically constant. Similar behavior is also observed for tactoids with homeotropic isotropic-nematic anchoring. While the average charge is well defined, as long as the defects constantly enter and leave the tactoid, instant topological charge s_t significantly fluctuates with time (Fig. 15c).

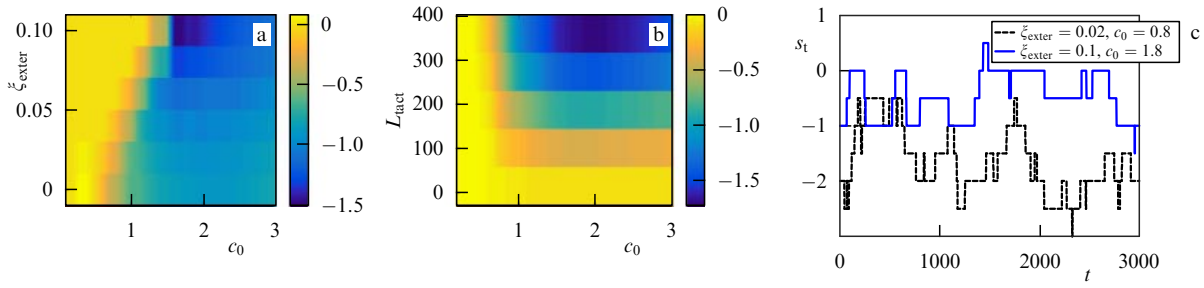

Figure 15. Topological charge for an isotropic tactoid in a nematic medium with planar IN anchoring. (a) Tactoid charge $\langle s_t \rangle$ vs. wall anchoring strength ξ_{exter} and mean bacteria concentration c_0. The tactoid size is fixed: $L_{\text{tact}} = 180$. (b) Tactoid charge $\langle s_t \rangle$ vs. tactoid size L_{tact} and mean bacteria concentration c_0. Here, the wall anchoring strength is fixed to $\xi_{\text{exter}} = 0.02$. (c) The dependence of s_t on time for $c_0 = 0.8$, $\xi_{\text{exter}} = 0.02$ and $c_0 = 1.8$, $\xi_{\text{exter}} = 0.1$. (Figure reproduced from Ref. [76] © Institute of Physics 2018.)

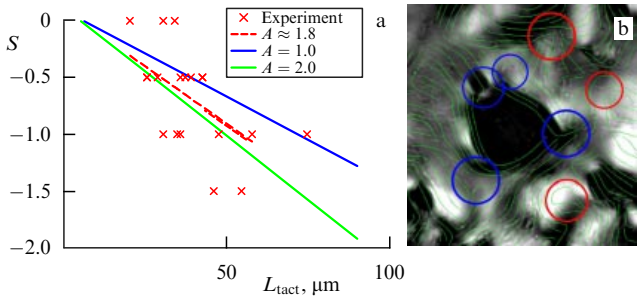

Figure 16. (Color online.) (a) Dependence of tactoid's topological charge on its size obtained from experiment (crosses) and simulations (solid lines). The activity of bacteria A, a product of bacterial concentration c_0 and dipole force strength, is extracted from the linear fit (dashed line) of the experimental data. The bacterial concentration in the experiment was 5×10^9 cells per cm^3. (b) Nematic configuration around a single tactoid in the experiments. Positive defects are highlighted with red circles, negative with blue circles. Negative defects decorate the IN interface, whereas positive defects are present in the bulk of the nematic phase. (Figure reproduced from Ref. [76] © Institute of Physics 2018.)

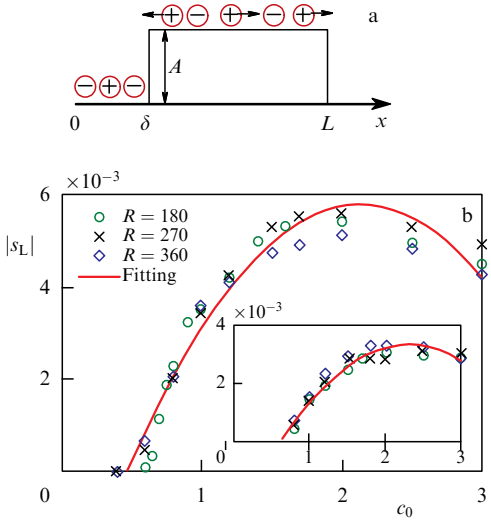

Figure 17. (a) Illustration of the one-dimensional system described by the Fokker–Plank model. (b) The magnitude of the tactoid's topological charge density vs. mean bacteria concentration for three different tactoid sizes. Main plot: isotropic tactoid with planar anchoring. Inset: isotropic tactoid with homeotropic anchoring. (Figure reproduced from Ref. [76] © Institute of Physics 2018.)

3.4.3 Experimental verification. The procedures for LLC sample preparation and data acquisition are described in a series of studies [33, 61, 76]. Experimental verification was performed with strain 1085 of motile bacteria *Bacillus subtilis* suspended in lyotropic liquid crystal disodium cromoglycate (DSCG) (Fig. 1). The microscopy images were acquired in the nearly cross-polarized regime, where the angle between a polarizer and an analyzer was slightly less than $\pi/2$. This regime allows simultaneous observation of both swimming bacteria and tactoids seen as dark areas (Fig. 5b).

Topological charges of 17 visible tactoids were determined by summing the topological charges of all defects around each tactoid. Analysis of the experimental data reveals that the magnitude of the total topological charge increases with the size of the tactoid, confirming the theoretical prediction (see Fig. 16a). Furthermore, the experiments confirmed that negative topological defects decorate the isotropic-nematic interface. In contrast, positive defects are found mostly in the bulk of the nematic phase (Fig. 16b).

3.4.4 Kinetic theory of charging. The onset of tactoid spontaneous charge can be attributed to different defect mobilities in active systems: $+1/2$ are mobile, whereas $-1/2$ are effectively immobile and only entrained by the moving ones [62, 63, 77]. The speed of $+1/2$ defects is at least 5 times larger than that of $-1/2$ defects (Fig. 11a). In order to enter or leave a tactoid, the defects need to overcome a potential barrier at the isotropic-nematic interface (Fig. 17a). Overall, the charging increases with the bacteria concentration, since the defect concentration itself is proportional to the concentration of bacteria [61]. However, at very large bacterial concentrations, the charging is overwhelmed by inter-defect repulsive interaction. The suggested mechanism resembles spontaneous charging of colloids in electrolytes [124–126] due to colloidal particle protonation and the transport of mobile protons into the solution.

This hypothesis can be further supported by a coarse-grained one-dimensional Fokker–Plank description for the probability distribution functions P^+ and P^- for positions of positive and negative defects (Fig. 17a). In this approach, it is assumed that the defects interact similarly to electrical charges (defects with the same topological charge repel, defects with opposite charges attract each other), and the interaction strength decays with the distance as $1/x$. Therefore, defect motion is affected by two competing factors: one is due to defect interaction and the other one due to a barrier on the tactoid surface. The corresponding Langevine equations for each individual defect can be written in the following form:

$$\partial_t x_i^+ = F'(x_i^+) + \mu\left(\sum_{j=0}^{N} \frac{1}{x_j^- - x_i^+} - \sum_{j=0,\, j\neq i}^{N} \frac{1}{x_j^+ - x_i^+}\right) + \xi^+ ,$$

$$\partial_t x_i^- = F'(x_i^-) + \mu\left(\sum_{j=0}^{N} \frac{1}{x_j^+ - x_i^-} - \sum_{j=0,\, j\neq i}^{N} \frac{1}{x_j^- - x_i^-}\right) + \xi^- , \tag{24}$$

where μ is the interaction strength, and $\xi^{\pm}$ are random forces with the magnitude $D^{\pm}$.

The sums in Eqn (24) can be replaced by integrals over the density distribution functions of positive and negative defects $P^{\pm}$: $\sum B_i = \int_0^{\infty} BP(x)\,\mathrm{d}x$. As a result, one obtains coupled Fokker–Plank equations for the probability density distribution functions $P^+(x,t)$ and $P^-(x,t)$:

$$\partial_t P^+(x,t) = D^+ \partial_x^2 P^+ - \partial_x\left[\left(-F'(x) + \mu\int_0^L \frac{P^+(x',t) - P^-(x',t)}{x - x'}\,\mathrm{d}x'\right) P^+(x,t)\right],$$

$$\partial_t P^-(x,t) = D^- \partial_x^2 P^- - \partial_x\left[\left(-F'(x) + \mu\int_0^L \frac{P^-(x',t) - P^+(x',t)}{x - x'}\,\mathrm{d}x'\right) P^-(x,t)\right]. \tag{25}$$

Here $D^{\pm}$ are the defect diffusivities, $D^+ \gg D^-$, μ is the inter-defect interaction strength, $F(x)$ describes a potential barrier at the isotropic-nematic interface, and L is the total size of the

system. The defect diffusivities are roughly proportional to the product of defect speed and its mean free path, which, in turn, depend on the concentration of bacteria. The formulation of the defects' motion as a diffusion-like process is justified by the fact that at sufficiently high bacterial concentrations the defect statistics can be well approximated by a Gaussian distribution (Fig. 11). An asymptotic solution for the tactoid charge density can be obtained from stationary Eqns (25) under the assumption of very large diffusivity D^+ for positive defects, i.e., $D^+ \gg D^-$, and weak defect interaction strength $\mu \ll 1$:

$$S = -P_0\delta\left[\exp\frac{A}{D^-} - 1\right] \times \left[1 - \frac{\mu\delta P_0 \exp\left(A/D^-\right)}{D^-}\left(\log\frac{L}{\delta} + 1\right)\right]. \quad (26)$$

Here, S is the tactoid topological charge density (charge per unit length), P_0 is the mean defect density in the system (assumed to be proportional to the bacterial concentration c), δ is the width of the isotropic-nematic interface, and A is the height of the potential barrier.

This model explains the spontaneous negative charging of the isotropic-nematic interface if one assumes $A > 0$. It will immediately imply accumulation of negative charge for negative tactoids and vice versa. The charge magnitude depends on the mean defect (or bacteria) concentration as $S \propto -C_0P_0 + C_1P_0^2$ with constants [7] $C_0 > C_1 > 0$.

The magnitude of the topological charge density, defined as the ratio of the tactoid topological charge to its length $|s_L|$ for different tactoid sizes and bacterial concentrations, is shown in Fig. 17b. One sees that for isotropic and nematic tactoids with planar and homeotropic IN anchoring, the tactoid topological charge density vs concentration is practically independent of the tactoid size and can be well approximated by a parabola, in agreement with the prediction from the Fokker–Plank model [Eqn (26)].

4. Conclusions

Here, we presented a brief overview of the role of topological defects in the spatiotemporal organization of active liquid crystals. Topological defects, acting as elementary excitations, can be used to control and manipulate these novel materials. Certainly, studies of topological defects and spatiotemporal behavior provide deep insight into fundamental mechanisms governing the dynamics of active matter. In addition, active liquid crystals may have intriguing applications as soft adaptive bio-inspired materials responding to physical and chemical stimuli, such as light, mechanical shear, airborne pollutants, and bacterial toxins (see review [128]).

Besides DSCG and other nontoxic lyotropic liquid crystals (e.g., Sunset Yellow FCF $C_{16}H_{10}N_2Na_2O_7S_2$, a food additive), many biological fluids, such as mucus [129], DNA solutions [130], and suspensions of viruses [131], often exhibit a liquid crystalline order. These liquids, especially mucus, are often relevant to human health. Mucus plays crucial roles in higher organisms, from preventing bacterial and viral infection and aiding fertilization to protecting the female reproductive tract. Since mucus anisotropy and heterogeneity depend on how mechanical stress is applied, it affects the motility of bacteria in a nontrivial way [132].

In the examples described above, swimming bacteria play the role of an 'active dopant'. A pure mimetic analog of living liquid crystal is highly desirable for many technological applications such as sensors. It can be done, in principle, by replacing bacteria with synthetic swimmers like catalytic gold-platinum (AuPt) nanorods [12] or other types of phoretic Janus particles, e.g., platinum-silica spheres [12]. Unfortunately, the chemical composition of lyotropic liquid crystals is generally not comparable to the chemical propulsion mechanism of AuPt nanorods. In addition to chemical propulsion, nanorods can be powered acoustically by ultrasound [134, 135]. Acoustically propelled nanorods can be easily transferred to the liquid crystalline environment. However, the inhomogeneous spatial distribution of the ultrasound intensity makes control of nanorod motion rather challenging. Besides chemically or acoustically propelled rods, spherical Janus particles can be driven in liquid crystals by an applied electric field due to self-electrophoresis [4, 136, 137].

So far, only nematic active liquid crystals have been explored. Further exploration of more ordered liquid crystalline phases such as smectics (layered) or cholesterics (chiral) is intriguing. However, preliminary experiments showed that bacteria do not exhibit mobility in smectic or cholesteric liquid crystals, likely due to increased viscosity in these phases.

As discussed above, point topological $\pm 1/2$ defects dominate the dynamics of active nematic liquid crystals. In addition to point defects, smectic liquid crystals exhibit textures of more complex singularities, such as focal conical domains (FCDs) and lamellar (plate-like) structures. FCDs are surfaces whose lines of curvature are circles [138]. The use of focal conical and lamellar domains opens an opportunity to control active matter by surface patterning [139] or a magnetic field [140]. For example, by interfacing an active nematic [32] with a smectic liquid crystal, one may reversibly turn well-developed active turbulence into a highly organized flow of liquid crystal by an applied magnetic field [140].

[7] The charge density decreases with the system size as $S \propto -\log(L/\delta)$. The logarithmic divergence of S with the system size is an artifact of the assumption that the interaction strength between defects is $1/x$. There are various ways to regularize the divergence. For example, one can introduce an exponential screening length similar to the Debye length due to a redistribution of defects [127].

Acknowledgments
This research was supported by the US National Science Foundation, grants DMR-1735700 and PHY-1707900.

References

1. Aranson I S *Phys. Usp.* **56** 79 (2013); *Usp. Fiz. Nauk* **183** 87 (2013)
2. Marchetti M C et al. *Rev. Mod. Phys.* **85** 1143 (2013)
3. Vicsek T, Zafeiris A *Phys. Rep.* **517** 71 (2012)
4. Lavrentovich O D *Current Opin. Colloid Interface Sci.* **21** 97 (2016)
5. Dombrowski C et al. *Phys. Rev. Lett.* **93** 098103 (2004)
6. Sokolov A, Aranson I S, Kessler J O, Goldstein R E *Phys. Rev. Lett.* **98** 158102 (2007)
7. Goldstein R E *Annu. Rev. Fluid Mech.* **47** 343 (2015)
8. Kantsler V et al. *eLife* **3** e02403 (2014)
9. Surrey T et al. *Science* **292** 1167 (2001)
10. Schaller V et al. *Nature* **467** 73 (2010)
11. Sumino Y et al. *Nature* **483** 448 (2012)
12. Paxton W F et al. *J. Am. Chem. Soc.* **126** 13424 (2004)
13. Palacci J et al. *Science* **339** 936 (2013)
14. Theurkauff I et al. *Phys. Rev. Lett.* **108** 268303 (2012)
15. Buhl J et al. *Science* **312** 1402 (2006)

16. Cavagna A et al. *Proc. Natl. Acad. Sci. USA* **107** 11865 (2010)
17. Ward A J et al. *Proc. Natl. Acad. Sci. USA* **105** 6948 (2008)
18. Karamouzas I, Skinner B, Guy S J *Phys. Rev. Lett.* **113** 238701 (2014)
19. Wensink H H et al. *Proc. Natl. Acad. Sci. USA* **109** 14308 (2012)
20. Sokolov A, Aranson I S *Phys. Rev. Lett.* **109** 248109 (2012)
21. Saintillan D, Shelley M J *Phys. Rev. Lett.* **100** 178103 (2008)
22. Aranson I S et al. *Phys. Rev. E* **75** 040901(R) (2007)
23. Saintillan D, Shelley M J *Compt. Rend. Phys.* **14** 497 (2013)
24. Sokolov A, Aranson I S *Phys. Rev. Lett.* **103** 148101 (2009)
25. López H M et al. *Phys. Rev. Lett.* **115** 028301 (2015)
26. Palacci J et al. *Sci. Adv.* **1** e1400214 (2015)
27. Ren L et al. *ACS Nano* **11** 10591 (2017)
28. Löwen H *Phys. Rep.* **237** 249 (1994)
29. Berg H C, Brown D A *Nature* **239** 500 (1972)
30. Takagi D et al. *Phys. Rev. Lett.* **110** 038301 (2013)
31. Weber C A et al. *Proc. Natl. Acad. Sci. USA* **112** 10703 (2015)
32. Sanchez T et al. *Nature* **491** 431 (2012)
33. Zhou S, Sokolov A, Lavrentovich O D, Aranson I S *Proc. Natl. Acad. Sci. USA* **111** 1265 (2014)
34. Zimmermann N et al. *Soft Matter* **11** 1547 (2015)
35. Schimansky-Geier L et al. *Phys. Lett. A* **207** 140 (1995)
36. Schweitzer F, Ebeling W, Tilch B *Phys. Rev. Lett.* **80** 5044 (1998)
37. Romanczuk P et al. *Eur. Phys. J. Spec. Top.* **202** 1 (2012)
38. Cates M E, Tailleur J *Annu. Rev. Condens. Matter Phys.* **6** 219 (2015)
39. Solon A P et al. *Phys. Rev. Lett.* **114** 198301 (2015)
40. Nardini C et al. *Phys. Rev. X* **7** 021007 (2017)
41. Aranson I S, Tsimring L S *Rev. Mod. Phys.* **78** 641 (2006)
42. Aranson I S et al. *Phys. Rev. Lett.* **84** 3306 (2000)
43. Clerc M G et al. *Nature Phys.* **4** 249 (2008)
44. Peruani F et al. *Phys. Rev. Lett.* **108** 098102 (2012)
45. Zhang H P et al. *Proc. Natl. Acad. Sci. USA* **107** 13626 (2010)
46. Narayan V, Ramaswamy S, Menon N *Science* **317** 105 (2007)
47. Aranson I S, Volfson D, Tsimring L S *Phys. Rev. E* **75** 051301 (2007)
48. Kudrolli A et al. *Phys. Rev. Lett.* **100** 058001 (2008)
49. Pawar A B, Kretzschmar I *Macromol. Rapid Commun.* **31** 150 (2010)
50. Bianchi E, Blaak R, Likos C N *Phys. Chem. Chem. Phys.* **13** 6397 (2011)
51. de Gennes P G, Prost J *The Physics of Liquid Crystals* (Intern. Ser. of Monographs on Physics, Vol. 83) (Oxford: Oxford Univ. Press, 1995)
52. Kléman M, Lavrentovich O D *Soft Matter Physics*: *an Introduction* (New York: Springer, 2007)
53. Kim Y-K, Shiyanovskii S V, Lavrentovich O D *J. Phys. Condens. Matter* **25** 404202 (2013)
54. Mushenheim P C et al. *Soft Matter* **10** 88 (2014)
55. Nazarenko V G et al. *Phys. Rev. Lett.* **105** 017801 (2010)
56. Zhou S at al. *New J. Phys.* **19** 055006 (2017)
57. Mushenheim P C et al. *Soft Matter* **11** 6821 (2015)
58. Mermin N D *Rev. Mod. Phys.* **51** 591 (1979)
59. Pismen L M *Vortices in Nonlinear Fields*: *From Liquid Crystals to Superfluids, from Non-equilibrium Patterns to Cosmic Strings* (Intern. Ser. of Monographs on Physics, Vol. 100) (New York: Oxford Univ. Press, 1999)
60. Abrikosov A A, Gorkov L P, Dzyaloshinski I E *Methods of Quantum Field Theory in Statistical Physics* (North Chelmsford, MA: Dover Publ., 2012)
61. Genkin M M, Sokolov A, Lavrentovich O D, Aranson I S *Phys. Rev. X* **7** 011029 (2017)
62. Giomi L et al. *Phys. Rev. Lett.* **110** 228101 (2013)
63. Pismen L M *Phys. Rev. E* **88** 050502(R) (2013)
64. Keber F C et al. *Science* **345** 1135 (2014)
65. Thampi S P, Golestanian R, Yeomans J M *Europhys. Lett.* **105** 18001 (2014)
66. Bodenschatz E, Pesch W, Kramer L *Physica D* **32** 135 (1988)
67. Ellis P W et al. *Nature Phys.* **14** 85 (2018)
68. Needleman D, Dogic Z *Nature Rev. Mater.* **2** 17048 (2017)
69. DeCamp S J et al. *Nature Mater.* **14** 1110 (2015)
70. Kamien R D *Rev. Mod. Phys.* **74** 953 (2002)
71. Nelson D R *Nano Lett.* **2** 1125 (2002)
72. Pairam E et al. *Proc. Natl. Acad. Sci. USA* **110** 9295 (2013)
73. Sokolov A, Zhou S, Lavrentovich O D, Aranson I S *Phys. Rev. E* **91** 013009 (2015)
74. Kumar A et al. *Mol. Cryst. Liquid Cryst.* **574** 33 (2013)
75. Trivedi R R et al. *Soft Matter* **11** 8404 (2015)
76. Genkin M M, Sokolov A, Aranson I S *New J. Phys.* **20** 043027 (2018)
77. Kawaguchi K, Kageyama R, Sano M *Nature* **545** 327 (2017)
78. Guo Y et al. *Adv. Mater.* **28** 2353 (2016)
79. Peng C et al. *Science* **354** 882 (2016)
80. Landau L D, Lifshitz E M *Fluid Mechanics* 2nd ed. (Amsterdam: Elsevier, 2013)
81. Köhler S, Schaller V, Bausch A R *Nature Mater.* **10** 462 (2011)
82. Saw T B et al. *Nature* **544** 212 (2017)
83. Malinverno C et al. *Nature Mater.* **16** 587 (2017)
84. Harvey C W, Alber M, Tsimring L S, Aranson I S *New J. Phys.* **15** 035029 (2013)
85. Wu Y et al. *Proc. Natl. Acad. Sci. USA* **106** 1222 (2009)
86. Volfson D et al. *Proc. Natl. Acad. Sci. USA* **105** 15346 (2008)
87. Ngo S et al. *Phys. Rev. Lett.* **113** 038302 (2014)
88. Gao T et al. *Phys. Rev. E* **92** 062709 (2015)
89. Ramaswamy S, Simha R A, Toner J *Europhys. Lett.* **62** 196 (2003)
90. Baskaran A, Marchetti M C *Phys. Rev. E* **77** 011920 (2008)
91. Bertin E et al. *New J. Phys.* **15** 085032 (2013)
92. Beris A N, Edwards B J *Thermodynamics of Flowing Systems*: *with Internal Microstructure* (Oxford Engineering Science Series, Vol. 36) (New York: Oxford Univ. Press, 1994)
93. Thampi S P, Golestanian R, Yeomans J M *Phys. Rev. Lett.* **111** 118101 (2013)
94. Thampi S P, Golestanian R, Yeomans J M *Phys. Rev. E* **90** 062307 (2014)
95. Blow M L, Thampi S P, Yeomans J M *Phys. Rev. Lett.* **113** 248303 (2014)
96. Giomi L *Phys. Rev. X* **5** 031003 (2015)
97. Vicsek T et al. *Phys. Rev. Lett.* **75** 1226 (1995)
98. Chaté H, Ginelli F, Montagne R *Phys. Rev. Lett.* **96** 180602 (2006)
99. Aranson I S, Tsimring L S *Phys. Rev. E* **71** 050901(R) (2005)
100. Peshkov A et al. *Phys. Rev. Lett.* **109** 268701 (2012)
101. Sokolov A, Rubio L D, Brady J F, Aranson I S *Nature Commun.* **9** 1322 (2018)
102. Thampi S P, Golestanian R, Yeomans J M *Phil. Trans. R. Soc. A* **372** 20130366 (2014)
103. Doostmohammadi A et al. *Nature Commun.* **7** 10557 (2016)
104. Hatwalne Y et al. *Phys. Rev. Lett.* **92** 118101 (2004)
105. Ramaswamy S *Annu. Rev. Condens. Matter Phys.* **1** 323 (2010)
106. Hernandez-Ortiz J P, Stoltz C G, Graham M D *Phys. Rev. Lett.* **95** 204501 (2005)
107. Guillamat P et al. *Phys. Rev. E* **94** 060602(R) (2016)
108. Yan W, Brady J F *J. Fluid Mech.* **785** R1 (2015)
109. Putzig E et al. *Soft Matter* **12** 3854 (2016)
110. Oza A U, Dunkel J *New J. Phys.* **18** 093006 (2016)
111. Aranson I S, Kramer L *Rev. Mod. Phys.* **74** 99 (2002)
112. Zhang R et al. *Nature Commun.* **7** 13483 (2016)
113. Tasinkevych M et al. *Soft Matter* **10** 2047 (2014)
114. Kim S, Karrila S J *Microhydrodynamics*: *Principles and Selected Applications* (North Chelmsford, MA: Dover Publ., 2013)
115. Krieger M S, Spagnolie S E, Powers T *Soft Matter* **11** 9115 (2015)
116. Smith C J, Denniston C *J. Appl. Phys.* **101** 014305 (2007)
117. Brochard F, de Gennes P G *J. Physique* **31** 691 (1970)
118. Tirado M M, de la Torre J G *J. Chem. Phys.* **73** 1986 (1980)
119. Zhou S et al. *Soft Matter* **10** 6571 (2014)
120. van Zon J, MacKintosh F C *Phys. Rev. Lett.* **93** 038001 (2004)
121. Kohlstedt K et al. *Phys. Rev. Lett.* **95** 068001 (2005)
122. Landau L D, Lifshitz E M, Pitaevskii L P *Statistical Physics* Pt. 1 (Oxford: Pergamon Press, 1980)
123. Kaznacheev A V, Bogdanov M M, Taraskin S A *JETP* **95** 57 (2002); *Zh. Eksp. Teor. Fiz.* **122** 68 (2002)
124. Hiemstra T, Van Riemsdijk W H, Bolt G H *J. Colloid Interface Sci.* **133** 91 (1989)
125. Behrens S H, Grier D G *J. Chem. Phys.* **115** 6716 (2001)
126. Sapozhnikov M V, Tolmachev Y V, Aranson I S, Kwok W-K *Phys. Rev. Lett.* **90** 114301 (2003)
127. Israelachvili J N *Intermolecular and Surface Forces* (Burlington, MA: Academic Press, 2011)
128. Bukusoglu E et al. *Annu. Rev. Chem. Biomol. Eng.* **7** 163 (2016)
129. Viney C, Huber A E, Verdugo P *Macromolecules* **26** 852 (1993)

130. Smalyukh I I et al. *Phys. Rev. Lett.* **96** 177801 (2006)
131. Dogic Z, Fraden S *Current Opin. Colloid Interface Sci.* **11** 47 (2006)
132. Figueroa-Morales N, Dominguez-Rubio L, Ott T L, Aranson I S *Sci. Rep.* **9** 9713 (2019)
133. Ebbens S J, Howse J R *Soft Matter* **6** 726 (2010)
134. Wang W et al. *ACS Nano* **6** 6122 (2012)
135. Wang W et al. *Angew. Chem. Int. Ed.* **53** 3201 (2014)
136. Lavrentovich O D, Lazo I, Pishnyak O P *Nature* **467** 947 (2010)
137. Hernàndez-Navarro S et al. *Angew. Chem.* **126** 10872 (2014)
138. Kléman M *J. Physique* **38** 1511 (1977)
139. Guo W, Herminghaus S, Bahr C *Langmuir* **24** 8174 (2008)
140. Guillamat P, Ignés-Mullol J, Sagués F *Proc. Natl. Acad. Sci. USA* **113** 5498 (2016)